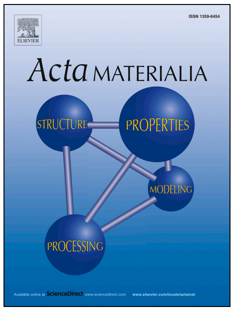

Dynamic shear deformation of a CrCoNi medium-entropy alloy with heterogeneous grain structures

Yan Ma, Fuping Yuan, Muxin Yang, Ping Jiang, Evan Ma, Xiaolei Wu

PII: S1359-6454(18)30117-4
DOI: 10.1016/j.actamat.2018.02.016
Reference: AM 14372

To appear in: *Acta Materialia*

Received Date: 16 November 2017
Revised Date: 6 February 2018
Accepted Date: 12 February 2018

Please cite this article as: Y. Ma, F. Yuan, M. Yang, P. Jiang, E. Ma, X. Wu, Dynamic shear deformation of a CrCoNi medium-entropy alloy with heterogeneous grain structures, *Acta Materialia* (2018), doi: 10.1016/j.actamat.2018.02.016.

This is a PDF file of an unedited manuscript that has been accepted for publication. As a service to our customers we are providing this early version of the manuscript. The manuscript will undergo copyediting, typesetting, and review of the resulting proof before it is published in its final form. Please note that during the production process errors may be discovered which could affect the content, and all legal disclaimers that apply to the journal pertain.

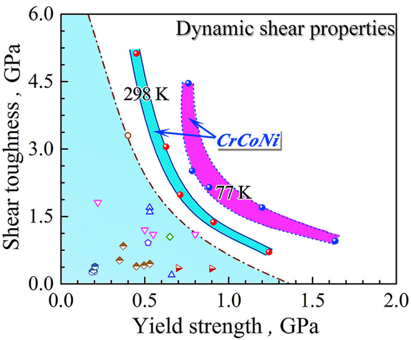
Dynamic shear properties
298 K
77 K
CrCoNi
Shear toughness , GPa
Yield strength , GPa
0.0
1.5
3.0
4.5
6.0
0.0
0.5
1.0
1.5
2.0

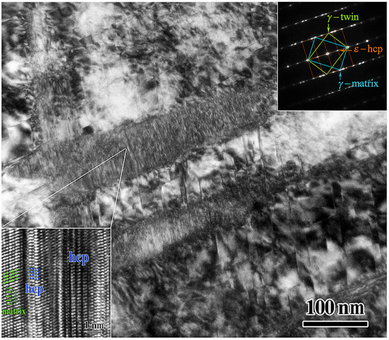
γ – twin
ε – hcp
γ – matrix
hcp
hcp
(111)
matrix
1 nm
100 nm

Dynamic shear deformation of a CrCoNi medium-entropy alloy with heterogeneous grain structures

Yan Ma[a,b], Fuping Yuan[a,b*], Muxin Yang[a], Ping Jiang[a], Evan Ma[c], and Xiaolei Wu[a,b]

[a]State Key Laboratory of Nonlinear Mechanics, Institute of Mechanics, Chinese Academy of Sciences, No.15, West Road, North 4th Ring, Beijing 100190, China

[b]School of Engineering Science, University of Chinese Academy of Sciences, Beijing 100190, China

[c]Department of Materials Science and Engineering, Johns Hopkins University, 3400 North Charles Street, Baltimore, MD 21218, USA

mayan@imech.ac.cn (Y. Ma), Tel.: 86-10-82543979.

mxyang@lnm.imech.ac.cn (M. X. Yang), Tel.: 86-10-82543217.

jping@imech.ac.cn (P. Jiang), Tel: 86-10-82544227.

ema@jhu.edu (E. Ma), Tel.: 1 410 516-8601.

xlwu@imech.ac.cn (X.L. Wu), Tel: 86-10-82543957.

Corresponding author: fpyuan@lnm.imech.ac.cn (F.P. Yuan) Tel.: 86-10-82544409

Abstract

Single-phase CrCoNi medium-entropy alloys (MEA) are emerging recently as an interesting class of metallic materials, but the dynamic response of this MEA at high strain rates remains unknown. Here we have produced this MEA with various heterogeneous microstructures, using cold rolling followed by annealing at various temperatures. The high-strain-rate response of the MEAs was characterized using hat-shaped specimens in Hopkinson-bar experiments. A combination of high dynamic shear yield strength and large uniform dynamic shear strain was observed, exceeding all other metals and alloys reported so far. Even better dynamic shear properties was revealed when the experiments were conducted at cryogenic temperature. The strong strain hardening under dynamic shear loading can be attributed to the dynamic grain refinement and deformation twinning that accompany the homogeneous shear deformation. When compared to room temperature, the efficiency of grain refinement was found to be enhanced at cryogenic temperature, with a higher density of multiple twins, stacking faults, Lomer-Cottrell locks, and hcp phase via phase transformation inside the grains, which could be responsible for the better dynamic shear properties under cryogenic environment.

Keywords: medium-entropy alloys; dynamic shear properties; grain refinement; Lomer-Cottrell locks; phase transformation

1. Introduction

High-entropy alloys (HEA) [1-14] and medium-entropy alloys (MEA) [15-20], containing multiple elements typically with equal molar fraction, have emerged recently as an interesting class of materials. This class of alloys can be solid solutions with a simple crystal structure, such as fcc, and the random distribution of multiple elements can reduce energy penalty for the formation of stacking fault (SF), rendering low stacking fault energy (SFE). Interestingly, the mechanical properties of fcc FeCrMnCoNi HEA and fcc CrCoNi MEA are better at cryogenic temperatures than at room-temperature, with a simultaneous enhancement in strength, ductility and fracture toughness, due to a transition of deformation mechanism from dislocation slip to deformation twinning [7,15].

However, HEA and MEA with coarse grains (CG) have a weakness in their relatively low room temperature yield strength. Thus severe plastic deformation (SPD) such as cold rolling (CR) has been applied to obtain increased yield strength in HEA and MEA [1,3,5,9]. Post-deformation annealing produces a multi-modal grain size distribution. Such a heterogeneous grain structure is known to result in a better combination of strength and ductility [21-30]. In our recent work [26,27], stress/strain partitioning and strain gradients have been found to play an important role during the tensile deformation in heterogeneous structures, resulting in back stresses that enhance extra strain hardening and uniform elongation. This strategy can also be used for metals and alloys with ultra-low SFE, such as HEAs and MEAs.

The un-dissipated plastic work leads to appreciable temperature rise such that the flow behaviors under dynamic loading are totally different from those under quasi-static conditions, and a clear understanding of the fundamental deformation mechanisms in metals and alloys exposed to high strain rate is critical to the designs of advanced crash relevant and impact-tolerant structures [31-35]. The thermal softening due to the adiabatic heating can facilitate strain localization, such as adiabatic shear band (ASB) [35-37], which is a precursor of the final failure. Thus, the microstructure evolution before and after the formation of ASB is critical for understanding the mechanical properties and the corresponding deformation mechanisms of metals and alloys subjected to impact loading [38-42]. The dynamic shear behaviors in homogeneous metal and alloys with CG, ultra-fine grains (UFG) or NG have been investigated extensively in the literature [35-40]. The CG metals are observed to have low yield strength, high critical strain for onset of ASB and high energy absorption under dynamic loading, while the UFG or NG metals are found to show high yield strength, low uniform shear strain and low energy absorption under dynamic loading. The normal strength-ductility trade-off under quasi-static conditions is found to still exist under dynamic shear loading for homogeneous microstructure. In this regards, the heterogeneous microstructure has the potential to achieve a better combination of strength-ductility even under high strain rate deformation, as suggested in our recent paper [42,43].

In the present study, we have designed heterogeneous grain structure through CR followed by annealing, and investigated mechanical properties upon impact loading. Moreover, how the hierarchical grain structure dynamically evolves upon the impact loading and how the microstructure evolution affects the overall dynamic shear properties are critical for the applications of this class of MEAs. In this work, a series of Hopkinson-bar experiments using hat-shaped specimens have been conducted on the MEA with various microstructures to investigate the dynamic shear properties under impact shear loading. Extraordinary dynamic shear properties have been observed, especially at cryogenic temperatures. The underlying deformation mechanisms are discussed using information from microstructural examinations at various controlled shear displacements.

2. Materials and experimental procedures

The equimolar CrCoNi MEA was produced via electromagnetic levitation melting in a high-purity argon atmosphere, and cast to ingots with a diameter of 120 mm and a height of 100 mm. The actual chemical composition of the ingots was determined to be 35.19Ni–35.67Cr–26.20Co (weight %). The ingots were first homogenized at 1473 K for 12 h, and then hot-forged into slabs with the thickness of 10 mm, at temperatures in between 1323 K and 1173 K. The slabs were then cold rolled into sheets with the final thickness of about 2.7 mm. The CR sheets were subsequently annealed, each at a different temperature, in the range of 873 to 1073 K, for 1 hour and immediately water quenched to obtain various heterogeneous microstructures.

The hat-shaped plate specimens have been machined from the sheets using a wire saw, with the impact direction perpendicular to the rolling direction. All specimens were mechanically polished prior to dynamic shear test in order to remove surface irregularities. The set-up for Hopkinson-bar experiments with hat-shaped plate specimens is displayed in Fig. 1(a), and the schematics of the hat-shaped specimens and the specimen holders are shown in Fig. 1(b). The cylindrical high strength maraging steel specimen holder was employed for two purposes: (1) it ensures pure shear deformation by constraining the lateral expansion of two legs for the hat-shaped specimens; (2) the shear displacements for interrupted "frozen" experiments are controlled by changing the height of the specimen holders. The hat-shaped set-up can facilitate the formation of ASB in the narrow concentrated shear zone, and the experimental details for the dynamic shear experiments by Hopkinson-bar technique can be found elsewhere [35,36,39-44]. The concentrated shear zone is marked by two white lines in Fig. 1, and the shear zone has a width of 0.2 mm and a height of 2 mm. The angle between the shear direction and the impact direction is only about 5^0, thus the deformation mode can be considered as nearly pure dynamic shear, and the measured total load can approximately be considered as the shear load [44]. Cryogenic temperature experiments (77 K) were conducted by immerging the specimen into liquid nitrogen for 10 minutes before dynamic shear tests. The impact velocities of the striker bar for the dynamic shear experiments were about 25 m/s and the nominal shear strain rates were as high as 8×10^4 /s.

Scanning electron microscope (SEM), electron backscattered diffraction (EBSD), transmission electron microscope (TEM) and high resolution electron microscope (HREM) have been used to characterize the microstructures before and after dynamic shear testing. The EBSD step size was 30 nm. Thin foils for TEM observations were cut from both the homogeneous shear zone away from the ASB and within the ASB zone, and then mechanically ground to about 50 μm thick and finally thinned by a twin-jet polishing facility using a solution of 5% perchloric acid and 95% ethanol at −25 ºC. The detailed procedures of sample preparation for SEM, EBSD can be found elsewhere [27,45].

3. Results and discussions

3.1 Microstructural characterization before dynamic shear tests

EBSD maps (Inverse pole figure, IPF) for the microstructures annealed at 1073, 973, 923 and 898 K are shown in Figs. 2a, 2b, 2c and 2d, respectively. The corresponding grain size distributions, plotted in terms of the area fraction, are shown in Fig. 2e. In Fig. 2e, only high-angle grain boundaries (HAGBs, with misorientation > 15^0) are considered and annealing twins are excluded when calculating the grain size. Moreover, Fig. 2f shows that the misorientation angle distributions have a strong preference for 60^0, indicating a large number of annealing twins. As expected, heterogeneous grain structures are observed for the samples annealed at various temperatures: all microstructures are composed of hierarchical grains with grain size on multiple levels. In other words, all microstructures are multimodal in grain size distribution. For example, the grain size ranges from submicron to about 27 μm for the microstructure annealed at 1073 K and the average grain size is 4.70 μm (using the linear intercept method). The grain size ranges from submicron to about 16 μm for the microstructure annealed at 973 K and the average grain size is 2.82 μm. The grain size ranges from submicron to about 15 μm for the microstructure annealed at 923 K and the average grain size is 2.63 μm. The microstructure annealed at 898 K has the grain size ranging from submicron to about 6 μm and the average grain size is 0.75 μm. Moreover, the smallest grains are observed to have the tendency to distribute at the grain boundaries (GBs) or triple-junctions of the large grains.

TEM images for the two microstructures annealed at 1073 and 898 K are shown in Fig. 3. As shown in the TEM bright-field image for the microstructure annealed at 1073 K (Fig. 3a), sharp GBs are well-known for recrystallized grains, and straight twin boundaries (TB) are clearly observed for the annealing twins (marked by green arrows). The inset of Fig. 3a is the selected area diffraction (SAD), clearly indicating the twin relationship. The density of dislocation is low in the grain interior due to the high-temperature annealing (1073 K). In contrast, high density of dislocations along with multiple twins (with much smaller twin boundary spacing, TBS, several tens of nm) are found in the grain interiors for the microstructure annealed at 898 K (Fig. 3c). The smaller grain size in the microstructure annealed at 898 K (Fig. 3b), and the higher density of substructures and dislocations in the grain interior, will result in much higher strength than that annealed at 1073 K.

3.2 Dynamic shear properties

The dynamic shear tests have been conducted on the CR-samples annealed at different temperatures (873–1073 K), in order to investigate the microstructure effect on the dynamic shear properties. The dynamic experiments have also been conducted at both room temperature (298 K) and cryogenic temperature (77 K) to study the environment temperature effect on the dynamic shear properties.

Figs. 4a and 4b display the shear stress-shear displacement curves of the samples annealed at various temperatures for the dynamic shear experiments conducted at room temperature (298 K) and cryogenic temperature (77 K), respectively. It is well known that the point at peak stress can be considered as the initiation point of the ASB according to the widely accepted maximum stress criterion for hat-shaped specimens [35,41,44]. Thus, the uniform shear strain can be estimated through dividing the shear displacement by the width of the shear zone before the maximum stress point. The corresponding shear stress-shear strain curves are displayed in Figs. 4c and 4d. The impact shear toughness can be estimated using the area under the shear stress-shear strain curves before the onset of ASB. Then, the uniform shear strain and the impact shear toughness as a function of the dynamic shear yield strength for this MEA, along with other data points for various metal and alloys [39,41,42,44,46-50], are plotted in Figs. 4e and 4f, respectively. As indicated, this MEA with heterogeneous grain structures has a better combination of dynamic shear properties over all the other metals and alloys reported earlier, offering an excellent candidate for impact-relevant structures. Moreover, this MEA possesses even better dynamic shear properties under cryogenic environment than those at room temperature, rendering it potentially applicable as structural material in the low-temperature environment.

It is observed that the uniform shear strain under dynamic shear loading decreases when the annealing temperature decreases. This means that the propensity of flow localization increases with decreasing annealing temperature. The susceptibility to ASB for a metal can be quantitatively expressed as [37,51]: $\chi_{ASB} = (a/m)\min\left\{1, \frac{1}{(n/m)+\sqrt{n/m}}\right\}$, where a is the non-dimensional thermal softening parameter which can be calculated by $a = (-\partial\sigma/\partial T)/\rho c$ (T is the temperature, ρ is the mass density, and c is the specific heat of the metal), n is the strain hardening exponent, and m is the strain rate sensitivity. An increased χ_{ASB} quantitatively indicates an increased propensity for flow localization. Thus, lower strain hardening ability and lower strain rate sensitivity will favor the flow localization. The grain/substructure size is smaller when the annealing temperature is lower, as indicated in Fig. 2. As we know, the microstructure with smaller grain/substructure size generally has lower strain hardening ability and higher strain rate sensitivity for fcc metals [33,52]. Lower strain hardening produces smaller uniform shear strain, while higher strain rate sensitivity discourages shear localization under dynamic shear loading based on the aforementioned equation. These two factors will be competing for the samples with smaller grain/substructure size. The strain hardening exponent and the strain rate sensitivity under dynamic loading for various microstructures of this MEA will be investigated later using a series of dynamic compression experiments at various strain rates, thus the quantitative correlation between these two parameters and the critical strain for onset of ASB must await the future work.

3.3 Microstructure evolution during the homogeneous dynamic shear deformation

In order to understand the deformation mechanisms for the superior dynamic shear properties of this MEA, the experiments were interrupted at controlled shear displacements for the sample annealed at 1073 K. The specimens are "frozen" at these pre-determined shear strain magnitudes for subsequent microstructure observation. The microstructures for the experiments conducted at room temperature and cryogenic temperature are both characterized and compared. For the experiments conducted at room temperature, the specimens are "frozen" at controlled shear displacements of 0.36, 0.73, and 1.28 mm, whereas the experiments are interrupted at shear displacements of 0.26, 0.62, and 1.02 mm for the experiments conducted at cryogenic temperature.

The IPF images at various shear displacements (0.36, 0.73, 1.28 mm) for the experiments conducted at room temperature are shown in Fig. 5a, while the IPF images at various shear displacements (0.26, 0.62, 1.02 mm) for the experiments conducted at cryogenic temperature are displayed in Fig. 5b. As indicated in Fig. 4, the ASB is not formed before these shear displacements (0.36, 0.73, 1.28 mm for room temperature experiments, 0.26, 0.62, 1.02 mm for cryogenic temperature experiments), thus uniform shear deformation can be assumed at these shear displacements, and the EBSD images in Figs. 5a and 5b can represent the microstructures experienced the homogeneous shear deformation. Figs. 5c and 5d display the corresponding misorientation angle distributions at various shear displacements for the experiments conducted at room temperature and cryogenic temperature, respectively. The grain sizes as a function of the homogeneous shear strain for the experiments conducted at both room temperature and cryogenic temperature are plotted in Fig. 5e. The grain sizes in Fig. 5e are estimated by only counting the GBs with misorientation angle large than 15^0 (HAGBs) without taking twins into account. As indicated, the grains are observed to be severely elongated along the shear direction and refined with increasing shear displacement for the experiments conducted at both room temperature and cryogenic temperature. This dynamic grain refinement along with homogeneous shear deformation is one of the origins for the strong strain hardening in the dynamic shear tests, as observed in Figs. 4c and 4d. It is interesting to note that the grain refinement is more severe for the experiments conducted at cryogenic temperature than those conducted at room temperature at the same applied shear strain, which could be one of the origins for the better dynamic shear properties under cryogenic environment, as observed in Figs. 4e and 4f. It is well known that the grain refinement can be either mediated by cells with dislocation walls or by strong interactions between dislocations and multiple deformation twins (DTs) [54]. As we know, the efficiency of grain refinement via strong interactions between dislocations and multiple DTs is generally higher than that via dislocation cells [54], which should be the origin of the particularly high efficiency of grain refinement for this MEA under dynamic shear loading due to the ultra-low stacking faults energy (SFE) [18].

The strain hardening due to this dynamic grain refinement is very similar to the hardening in TWIP steels by DTs (also called to dynamic H-P effect for TWIP steels) [53]. And the strain hardening of grain refinement can be roughly estimated based on the average grain size before and after shear deformation and the coefficient of the Hall-Petch relation: $\Delta\tau = \Delta\sigma / \sqrt{3} = (K_{HP}\bar{d}_{after}^{-1/2} - K_{HP}\bar{d}_{before}^{-1/2}) / \sqrt{3}$. The coefficient of the Hall-Petch relation for this MEA has been estimated to be about 500 MPa.μm$^{1/2}$ using our tensile experimental data on the samples with different average grain sizes. Thus, the strain hardening due to the grain refinement during the dynamic shear loading can be roughly estimated to be about 200 MPa for the experiments conducted at both temperatures, which is the main contributor to the total strain hardening observed in the experiments (Figs. 4c and 4d). Based on the misorientation angle distributions, the strong preference for 60^0 in the undeformed microstructure is weakened during the homogenous shear deformation, while a less obvious preference of 60^0 is still observed at the shear displacements of 1.02 and 1.28 mm for the dynamic shear experiments at room temperature and cryogenic temperature, respectively. These observations are in contrast with the random misorientations observed within ASB, which is induced by grain refinement through dynamic recrystallization (DRX) at high temperature [35,40-42]. The lowering fraction of 60^0 misorientation angle during the shear deformation could be due to the interaction between the dislocations and the coherent TBs.

Deformation twinning has in fact been reported for this CrCoNi MEA with grains ranging from 5 to 50 μm in quasi-static tensile tests and fracture toughness tests [15], while grain refinement with HAGBs was not reported under quasi-static tensile loading for this grain range in this MEA [15]. In order to illustrate the other strain hardening mechanism in the grain interior besides the grain refinement, TEM bright-field images of the homogeneous shear deformation zone (the images are taken away from the ASB zone) after the dynamic shear experiments conducted at room temperature are displayed in Fig. 6. As indicated, numerous DTs (including occasional multiple twins, as shown in the inset of Fig. 6a) are observed and the TBS is observed to be as small as ~ 50 nm in the grain interior. A high density of dislocations are also observed in the areas adjacent to the TBs (Fig. 6b), indicating strong interactions between the dislocations and the TBs. As summarized in the previous study [55], four possible dislocation-TB reaction processes have been proposed in fcc metals and two of them involve the formation of immobile dislocation locks for strengthening and strain hardening. Thus, besides the dynamically grain refinement, the excellent dynamic shear properties observed for this MEA can also be due to the dislocation accumulation near the TBs for the experiments conducted at room temperature.

It is well known that an increase in strain rate has similar effect on deformation mechanisms as a decrease in deformation temperature, and vice versa, and the combined effects of strain rate ($\dot{\varepsilon}$) and deformation temperature (T) on the deformation mechanisms can often be represented by a single parameter, namely the Zener-Hollomon parameter (Z) defined as [56]: $Z = \dot{\varepsilon}\exp(Q/RT)$, where R is the gas constant and Q is the related activation energy for deformation. The high strain rate and the low temperature (as the case in the present study) generally represent the extreme deformation conditions, under which some unique deformation mechanisms may occur. In order to illustrate the detailed microstructure mechanisms in the grain interior for the strain hardening besides the grain refinement, bright-field

TEM images for the homogeneous dynamic shear deformation zone are also provided for the experiments conducted at cryogenic temperature, as shown in Fig. 7. Multiple twinning is regularly observed for the experiments conducted at cryogenic temperature (Fig. 7b). Previous research have shown that multiple twinning can induce higher strength and stronger strain hardening than single DTs [18,57,58]. The multiple twinning network can present more barriers for dislocation motion to contribute to the higher strength, and the network can also provide adequate pathways for easy glide and cross-slip of dislocations to accommodate significant plastic deformation for stronger strain hardening [18,57,58]. Besides the high density of multiple DTs, a high density of SFs are also observed in the experiments conducted at cryogenic temperature. Again, this is rooted in the low SFE of this MEA, which leads to profuse partial dislocations.

HREM images are also provided in Fig. 8 to show the deformation mechanisms in detail at atomic level for the experiments conducted at cryogenic temperature. TBs, SFs and dislocations at TBs can be clearly observed in the grain interior (Fig. 8a). Several Lomer-Cottrell (L-C) locks are also formed in the grain interior due to the reaction of leading partials from two different slip planes, and this scenario is seen in the high resolution views in Fig. 8b (highlighted by arrows). High density of extended dislocations exist on two 60^0 inter-crossing (111) planes, again due to the low SFE of this MEA [18], which leads to a high probability for the formation of L-C locks. These dissociated dislocations have been proposed to either originate from GBs or from the cross-slip of dislocations in the grain interior [59,60]. It have been reported that L-C locks can play critical role in the strain hardening of fcc metals [59,60,61], which is supported previously by both experiments and molecular dynamics (MD) simulations. The effectiveness of strain hardening for L-C locks derives from their capability to accumulate dislocations. Four dislocation segments are pinned by each L-C lock, and the length of the L-C lock is usually short, akin to a pinning point. The previous paper has shown that the elevated strengthening/hardening for L-C lock is similar to Orowan's strengthening/hardening by using an orientation dependent line tension model [61]. It can be found that significant strengthening/hardening can be induced when the distance between locks is small; in other words, high strengthening/hardening is achieved when the density of L-C locks is high in the grain interior. The density of L-C locks is lower than the density of SFs, which can still contribute to the strain hardening for the present experiments conducted at 77 K.

Numerous SFs with spacing less than several nm are also seen on multiple {111} planes in the grain interior (Fig. 7a, Fig. 8c). Although the effects of SFs on the strengthening and strain hardening may not be as strong as TBs [55,57], the high density of SFs itself can still contribute to the strengthening and the strain hardening according to previous research [62], in which SFs are also considered as barriers to dislocation motion and can accumulate dislocations around them. As indicated in Fig. 8c, phase transformation from fcc phase to hcp phase is also occasionally observed due to the successive formation and the overlapping of SFs at every other {111} plane. This phase transformation from fcc phase to hcp phase has also been recently reported in this MEA [63], in the Co-27Cr-5Mo-0.05C HEA [64] and in the

Fe-Mn30-Co10-Cr10 HEA [14] at large strain levels. The lamellar structures of hcp phase and the phase boundaries would be effective barriers for further dislocation slip since either <c> or <c+a> dislocations are required for transmission of edge dislocations into the hcp phase, and the activation of these dislocation types typically requires very high critical resolved shear stress. Thus, this strain-induced formation of hcp ε-martensite phase is very similar to the TRIP effect as frequently reported in high-Mn austenitic steels [65], which can result in strong strain hardening for sustaining large uniform elongations. It is well known that the dominant deformation mechanism can be switched between phase transformation and deformation twins, or a mixture of the two, by regulating the SFE through tailoring the Mn content in TRIP/TWIP steels [65]. Our MEA has lower SFE [18] when compared to the equiatomic CrMnFeCoNi HEA, thus a mixture of deformation twins and TRIP effect can be observed in this MEA, in contrast to the deformation twins only in the CrMnFeCoNi HEA [7]. Thus, the better dynamic shear properties for the high-strain-rate dynamic shear experiments conducted at cryogenic temperature should also be partially attributed to higher density of multiple twins, SFs, Lomer-Cottrell locks and hcp phase by phase transformation inside the grains. Since the densities of multiple twins and stacking faults are much higher compared to those of Lomer-Cottrell locks and hcp phase, and the strengthening and strain hardening effects of TBs should be much stronger compared to those of SFs [55,57], the sequence of importance of the aforementioned four different factors for strain hardening should be as follows: (i) multiple twins, (ii) SFs, (iii, iv) Lomer-Cottrell locks and phase transformation.

According to our two recent review papers [66,67], the mechanical properties in heterogeneous structures can be optimized through two factors: (i) high density of domain interfaces (the interfaces between hard domain and soft domain); (ii) maximizing strain partitioning and strain gradients between heterogeneous domains, which can be fulfilled by increasing strength difference between domains. Based the current results and the inspiration from these two review papers [66,67], the mechanical properties of this MEA could be further optimized by creating a wider range of grain size distribution in the future work, which might be fulfilled by CR under cryogenic temperature and subsequent proper annealing.

3.4 Temperature rise during the homogeneous dynamic shear deformation

During the dynamic shear process, the shear zone (200 μm width) can be considered as a homogeneous shear deformation zone before the onset of ASB, and the deformation can be approximately considered as an adiabatic process. Thus, the temperature rise during the homogeneous dynamic shear deformation due to the plastic dissipation work within the homogeneous shear zone can be estimated as [39,41]: $\Delta T = \frac{\eta}{\rho C_v}\int \tau d\gamma_p$, where ρ is the mass density, C_v is the heat capacity, η is the Taylor-Quinnery coefficient for plastic work converted to heat (commonly $\eta = 0.85$), γ_p is the plastic shear strain, and τ is the shear stress. For this MEA, ρ is measured to be 11.19 g/cm^3 and C_v can be approximately taken as 540 J/kg [68].

Based on this equation, the temperature rise for all experiments conducted at room temperature and cryogenic temperature can be calculated by utilizing the dynamic shear stress-shear strain curves in Figs. 4c and 4d, and the corresponding temperature rise vs. the homogeneous shear strain curves are displayed in Figs. 9a and 9b. This relates the temperature rises at various shear displacements to the microstructure evolution (the dynamic grain refinement evolution along with the shear deformation, as shown in Fig. 5) for the experiments conducted at room temperature and cryogenic temperature. The temperature rises are 126, 344 and 708 K at shear displacements of 0.36, 0.73 and 1.28 mm, respectively, for the experiments conducted at room temperature, whereas the temperature rises are 148, 315 and 579 K at shear displacements of 0.26, 0.62 and 1.02 mm, respectively, for the experiments conducted at cryogenic temperature. It should be noted that the dynamic grain refinement is achieved due to the large shear deformation with assistance of temperature rise at the shear zone. As shown, the temperature rise is lower than 300 K when the homogeneous shear strain is lower than 3. But the temperature rise can be as high as 720 K when the homogeneous shear strain reaches 6. As indicated in Figs. 4c and 4d, strong hardening is observed before the shear strain of 3 (stage I) for the sample annealed at 1073 K, while a plateau of shear flow stress is found after the shear strain of 3 (stage II). This observed trend could be due to the competition between the strong strain hardening from microstructural evolution (grain refinement, deformation twins, SFs, L-C locks, phase transformation) and thermal softening due to adiabatic temperature rise. Stage I is controlled by the strain hardening since the adiabatic temperature rise is low in this stage. The thermal softening can cancel out the strain hardening effect from the microstructural refinement in stage II since the adiabatic temperature rise is as high as 720 K. The cryogenic environment can reduce the actual temperature in the shear zone, thus weakening the thermal softening effect and resulting in better dynamic shear properties for the experiments conducted at cryogenic temperature.

3.5 Characteristics of ASB

Moreover, it is well known that the shear deformation will be concentrated in a thin shear band (generally with width about several to several tens of μm) once ASB is formed, and the shear strain within the ASB can generally be one order of magnitude higher than the nominal homogeneous shear strain, thus temperature rise within the ASB will be even higher. The high shear deformation magnitude and the high temperature rise within the ASB generally result in DRX in ASB. The characteristics of the ASB at the shear displacement of 2.0 mm for the sample annealed at 1073 K are displayed in Fig. 10. These images include the SEM images for the ASB zone, the IPF images and the TEM dark-field images for the ASB zone. Fig. 10a show the corresponding images for the experiment conducted at room temperature, whereas Fig. 10b displays the corresponding images for the experiment conducted at cryogenic temperature. The grain size distributions within ASB are displayed in Fig. 10c, and the corresponding misorientation angle distributions of the ASB zone are shown in Fig. 10d. Unlike the elongated grains in the homogeneous shear deformation zone, the grains in the ASB are equiaxed, signifying DRX. The grain size is refined to about 300 nm in the ASB for the experiments conducted both at room temperature and cryogenic temperature. The SAD patterns (as shown in the insets of Figs. 10a and 10b for the TEM images) clearly display random misorientation angles (as confirmed by Fig. 10d), which is a typical characteristic of DRX grains due to the high temperature rise and the severe plastic strain in the ASB.

According to Figs. 10a and 10b, the widths of the ASB for the experiments conducted at room temperature and cryogenic temperature are 12.5 and 6.4 μm, respectively. The smaller width of the ASB for the experiments at cryogenic temperature indicates that the shear deformation is more concentrated in cryogenic environment. A quantitative description for calculating the width of the ASB has been proposed according to the perturbation analysis of the uniform solutions for the governing equation of the ASB [69]: $\delta \approx 2(\frac{kT}{\tau\dot{\gamma}})^{1/2}$, where T is the temperature within the ASB, τ and $\dot{\gamma}$ are the shear stress and the shear strain rate within the ASB, respectively. k is the thermal conductivity. For this MEA, k can be approximately taken as 60 W/(K.m) [42,68]. The shear stress can be taken from the maximum stress of the curves in Figs. 4a and 4b. The actual shear strain rate within the ASB is generally one order of magnitude higher than the nominal shear rate [36,40], which can be calculated from the strain gage signal of the reflected wave. By comparing the width of ASB (12.5 μm for room temperature, 6.4 μm for cryogenic temperature) and the thickness of the whole shear zone (200 μm), the real shear strain rate within the ASB can be estimated to be about 16 times and 31 times of the nominal shear rate for the room temperature and cryogenic temperature experiments, respectively. As mentioned earlier, the temperature within the ASB is generally much higher than the temperature within the homogeneous shear deformation zone. Thus we take 1500 ℃ (1773 K, close to the melting temperature of this MEA) as the temperature within ASB, for a rough estimate of the ASB width. Based on the aforementioned equation, the widths of ASB have been roughly estimated to be 21 μm and 15 μm for the experiments conducted at room temperature and cryogenic temperature, respectively. This estimate is in reasonable agreement with the experimental observations (12.5 μm for room temperature, 6.4 μm for cryogenic temperature), as Wright [70] has indicated that the agreement of experimental results with the theoretical predictions is usually within a factor of two.

4. Concluding remarks

In the present study, the dynamic shear properties of the CrCoNi MEA have been investigated using a series of Hopkinson-bar experiments and hat-shaped specimens at both room temperature and cryogenic temperature, and the underlying deformation mechanisms have also been revealed by utilizing the "frozen" experiments and subsequent microstructure observations. The main findings are summarized as follows:

(1) Superior dynamic shear properties, in terms of a combination of dynamic shear strength and uniform dynamic shear strain, have been found for this MEA, exceeding all other metals and alloys investigated so far. The dynamic shear properties of this MEA are found to be even better when the experiments were conducted at cryogenic temperature.

(2) The excellent dynamic shear properties can be mainly attributed to the dynamically grain refinement along with the dynamic shear deformation. And the better dynamic shear properties at cryogenic temperature can be attributed to the more efficient grain refinement.

(3) Besides grain refinement, deformation twins and strong interactions between the dislocations and TBs also contribute partly to the strain hardening under dynamic shear loading at room temperature. Higher density of multiple twins, SFs, Lomer-Cottrell locks and phase transformation to hcp phase were observed in the grain interiors for the experiments conducted at cryogenic temperature, which could contribute to the better dynamic shear properties under cryogenic environment.

Acknowledgements

The work was supported by the National Key R&D Program of China [grant number 2017YFA0204402]; the National Natural Science Foundation of China [grant numbers 11472286, 11672313, 11790293, 11572328, 51701228, and 51601204], and the Strategic Priority Research Program of the Chinese Academy of Sciences [grant numbers XDB22040503].

References

[1] J.W. Yeh, S.K. Chen, S.J. Lin, J.Y. Gan, T.S Chin, T.T. Shun, C.H. Tsau, S.Y. Chang, Nanostructured high-entropy alloys with multiple principal elements: novel alloy design concepts and outcomes, Adv. Eng. Mater. 6 (2004) 299-303.

[2] B. Cantor, I.T.H. Chang, P. Knight, A. J. B. Vincent, Microstructural development in equiatomic multicomponent alloys, Mater. Sci. Eng. A 375 (2004) 213-218.

[3] W.H. Liu, Y. Wu, J.Y. He, T.G. Nieh, Z.P. Lu, Grain growth and the Hall–Petch relationship in a high-entropy FeCrNiCoMn alloy, Scr. Mater. 68 (2013) 526-529.

[4] A.J. Zaddach, C. Niu, C.C. Koch, D.L Irving, Mechanical properties and stacking fault

energies of NiFeCrCoMn high-entropy alloy, JOM 65 (2013) 1780-1789.

[5] F. Otto, A. Dlouhý, C. Somsen, H. Bei, G. Eggeler, E.P. George, The influences of temperature and microstructure on the tensile properties of a CoCrFeMnNi high-entropy alloy, Acta Mater. 61 (2013) 5743-5755.

[6] Y.P. Lu, Y. Dong, S. Guo, L. Jiang, H.J. Kang, T.M. Wang, B. Wen, Z.J. Wang, J.C. Jie, Z. Q. Cao, H. H. Ruan, T.J. Li, A promising new class of high-temperature alloys: eutectic high-entropy alloys, Sci. Rep. 4 (2014) 6200.

[7] B. Gludovatz, A. Hohenwarter, D. Catoor, E.H. Chang, E.P. George, R.O. Ritchie, A fracture-resistant high-entropy alloy for cryogenic applications. Science 345 (2014) 1153-1158.

[8] Y. Zhang, T.T. Zuo, Z. Tang, M. C. Gao, K.A. Dahmen, P.K. Liaw, Z.P. Lu, Microstructures and properties of high-entropy alloys, Prog. Mater. Sci. 61 (2014) 1-93.

[9] B. Schuh, F. Mendez-Martin, B. Völker, E.P. George, H. Clemens, R. Pippan, A. Hohenwarter, Mechanical properties, microstructure and thermal stability of a nanocrystalline CoCrFeMnNi high-entropy alloy after severe plastic deformation, Acta Mater. 96 (2015) 258-268.

[10] Y. Zou, H. Ma, R. Spolenak, Ultrastrong ductile and stable high-entropy alloys at small scales, Nat. commun. 6 (2015) 7748.

[11] Y.F. Ye, Q. Wang, J. Lu, C.T. Liu, Y. Yang, High-entropy alloy: challenges and prospects, Mater. Today 19 (2015) 349-362.

[12] Z. Zhang, M.M. Mao, J. Wang, B. Gludovatz, Z. Zhang, S.X. Mao, E.P. George, Q. Yu, R.O. Ritchie, Nanoscale origins of the damage tolerance of the high-entropy alloy CrMnFeCoNi, Nat. commun. 6 (2015) 10143.

[13] J.Y. He, H. Wang, H.L. Huang, X.D. Xu, M.W. Chen, Y. Wu, X.J. Liu, T.G. Nieh, K. An, Z.P. Lu, A precipitation-hardened high-entropy alloy with outstanding tensile properties. Acta Mater. 102 (2016) 187-196.

[14] Z. Li, K.G. Pradeep, Y. Deng, D. Raabe, C.C. Tasan, Metastable high-entropy dual-phase alloys overcome the strength–ductility trade-off, Nature 534 (2016) 227-230.

[15] B. Gludovatz, A. Hohenwarter, K.V. Thurston, H. Bei, Z. Wu, E.P. George, R.O. Ritchie, Exceptional damage-tolerance of a medium-entropy alloy CrCoNi at cryogenic temperatures, Nat. commun. 7 (2016) 10602.

[16] Z. Wu, H. Bei, F. Otto, G.M. Pharr, E.P. George, Recovery, recrystallization, grain growth and phase stability of a family of FCC-structured multi-component equiatomic solid solution alloys, Intermetallics 46 (2014) 131-140.

[17] Z. Wu, H. Bei, G.M. Pharr, E.P. George, Temperature dependence of the mechanical properties of equiatomic solid solution alloys with face-centered cubic crystal structures. Acta Mater. 81 (2014) 428-441.

[18] Z.J. Zhang, H.W. Sheng, Z.J. Wang, B. Gludovatz, Z. Zhang, E.P. George, Q. Yu, S.X. Mao, R.O. Ritchie, Dislocation mechanisms and 3D twin architectures generate exceptional strength-ductility-toughness combination in CrCoNi medium-entropy alloy. Nat. commun.8 (2017) 14390.

[19] Y.L. Zhao, T. Yang, Y. Tong, J. Wang, J.H. Luan, Z.B. Jiao, D. Chen, Y. Yang, A. Hu, C.T. Liu,

J.J. Kai, Heterogeneous precipitation behavior and stacking-fault-mediated deformation in a CoCrNi-based medium-entropy alloy, Acta Mater. 138 (2017) 72-82.

[20] J. Miao, C.E. Slone, T.M. Smith, C. Niu, H. Bei, M. Ghazisaeidi, G.M. Pharr, M.J. Mills, The evolution of the deformation substructure in a Ni-Co-Cr equiatomic solid solution alloy, Acta Mater. 132 (2017) 35-48.

[21] Y.M. Wang, M.W. Chen, F.H. Zhou, E. Ma, High tensile ductility in a nanostructured metal, Nature 419 (2002) 912-915.

[22] K. Lu, L. Lu, S. Suresh, Strengthening materials by engineering coherent internal boundaries at the nanoscale. Science 324 (2009) 349-352.

[23] P.V. Liddicoat, X.Z. Liao, Y.H. Zhao, Y.T. Zhu, M.Y. Murashkin, E.J. Lavernia, R.Z. Valiev, S.P. Ringer, Nanostructural hierarchy increases the strength of aluminium alloys, Nature Commun. 1, (2009) 63.

[24] D. Raabe, D. Ponge, O. Dmitrieva, B. Sander, Nanoprecipitate-hardened 1.5 GPa steels with unexpected high ductility, Scr. Mater. 60 (2009) 1141-1144.

[25] G. Liu, G.J. Zhang, F. Jiang, X.D. Ding, Y.J. Sun, J. Sun, E. Ma, Nanostructured high-strength molybdenum alloys with unprecedented tensile ductility, Nature Mater. 12(2009) 344–350.

[26] X.L. Wu, P. Jiang, L. Chen, F.P. Yuan, Y.T. Zhu, Extraordinary strain hardening by gradient structure, Proc. Natl. Acad. Sci. USA 111 (2014) 7197–7201.

[27] X.L. Wu, M.X. Yang, F.P. Yuan, G.L. Wu, Y.J. Wei, X.X. Huang, Y.T. Zhu, Heterogeneous lamella structure Unites ultrafine-grain strength with coarsegrain ductility, Proc. Natl. Acad. Sci. USA 112 (2015) 14501-14505.

[28] X.L. Wu, F.P. Yuan, M.X. Yang, P. Jiang, C.X. Zhang, L. Chen, Y.G. Wei, E. Ma, Nanodomained nickel unite nanocrystal strength with coarse-grain ductility, Scientific Reports 5 (2015) 11728.

[29] Y.J. Wei, Y.Q. Li, L.C. Zhu, Y. Liu, X.Q. Lei, G. Wang, Y.X. Wu, Z.L. Mi, J.B. Liu, H.T. Wang, H.J. Gao Evading the strengthductility trade-off dilemma in steel through gradient hierarchical nanotwins, Nat Commun. 5 (2014) 3580.

[30] T.H. Fang, W.L. Li, N.R. Tao, K. Lu, Revealing extraordinary intrinsic tensile plasticity in gradient nano-grained copper, Science 331 (2011) 1587–1590.

[31] C. Zener, J.H. Hollomon, Effect of strain rate upon plastic flow of steel, J Appl. Phys. 15 (1944) 22-32.

[32] S. Nemat-Nasser, W.G. Guo, Thermomechanical response of DH-36 structural steel over a wide range of strain rate and temperatuers, Mech. Mater. 35 (2003) 1023-1047.

[33] Q. Wei, Strain rate effects in the ultrafine grain and nanocrystalline regimes influence on some constitutive responses, J Mater. Sci. 42 (2007) 1709-1727.

[34] T. Suo, Y.L. Li, F. Zhao, X.L. Fan, W.G. Guo, Compressive behavior and rate-controlling mechanisms of ultrafine grained copper over wide temperature and strain rate ranges, Mech. Mater. 61 (2013) 1-10.

[35] A. Mishra, M. Martin, N.N. Thadhani, B.K. Kad, E.A. Kenik, M.A. Meyers, High-strain rate response of ultra-fine-grained copper, Acta. Mater. 56 (2008) 2770-2783.

[36] M.A. Meyers, Dynamic Behavior of Materials, Wiley-Interscience, New York, USA (1994) 323-326.

[37] Q. Wei, L. Kecskes, T. Jiao, K.T. Hartwig, K.T. Ramesh, E. Ma, Adiabatic shear banding in ultrafine-grained Fe processed by severe plastic deformation, Acta Mater. 52 (2004) 1859-1869.

[38] M.A. Meyers, G. Subhash, B.K. Kad, L. Prasad, Evolution of microstructure and shear-band formation in α-hcp titanium, Mech. Mater. 17 (1994) 175-193.

[39] Y. Yang, F. Jiang, B.M. Zhou, X.M. Li, H.G. Zheng, Q.M. Zhang, Influence of shock prestraining on the formation of shear localization in 304 stainless steel, Mater. Sci. Eng. A 528 (2011) 2787-2794.

[40] F.P. Yuan, P. Jiang, X.L. Wu, Annealing effect on the evolution of adiabatic shear band under dynamic shear loading in ultra-fine-grained iron, International Journal of Impact Engineering 50 (2012) 1-8.

[41] J.X. Xing, F.P. Yuan, X.L. Wu, Enhanced quasi-static and dynamic shear properties by heterogeneous gradient and lamella structures in 301 stainless steels. Mater. Sci.Eng. A 680 (2017) 305-316.

[42] F.P. Yuan, X.D. Bian, P. Jiang, M.X. Yang, X.L. Wu, Dynamic shear response and evolution mechanisms of adiabatic shear band in an ultrafine-grained austenite-ferrite duplex steel, Mech. Mater. 89 (2015) 47-58.

[43] X.D. Bian, F.P. Yuan, Y.T. Zhu, X.L. Wu, Gradient structure produces superior dynamic shear properties, Materials Research Letters 5 (2017) 501-507.

[44] Q. Xue, G.T. Gray III, B.L. Henrie, S.A. Maloy, S.R. Chen, Influence of shock prestraining on the formation of shear localization in 304 stainless steel, Metall. Mater. Trans. A 36 (2005) 1471-1486.

[45] M.X. Yang, F.P. Yuan, Q.G. Xie, Y.D. Wang, E. Ma, X. L. Wu, Strain hardening in Fe-16Mn-10Al-0.86C-5Ni high specific strength steel, Acta Mater. 109 (2016) 213-222.

[46] Q. Xue, G.T. Gray III, Development of adiabatic shear bands in annealed 316L stainless steel: Part I. Correlation between evolving microstructure and mechanical behavior. Metall Mater. Trans. A 37A (2006) 2435-2446.

[47] V.A. Pushkov, A.V. Yurlov, A.M. Podurets, A. Kal'manov, E. Koshatova, Study of adiabatic localized shear in metals by split Hopkinson pressure bar method, EPJ Web of Conferences 10 (2010) 00029.

[48] V.A. Pushkov, A.V. Yurlov, A.M. Podurets, A.N. Tsibikov, M.I. Tkachenko, A.N. Balandina, Effect of preloading on the formation of adiabatic localized shear in copper. Combustion, explosion, and shock waves 49 (2013) 620-624.

[49] U. Hofmann, E. El-Magd, Behaviour of Cu-Zn alloys in high speed shear tests and in chip formation processes. Mater. Sci. Eng. A 395 (2005) 129-140.

[50] Y.B. Gu, V.F. Nesterenko, Dynamic behavior of HIPed Ti-6Al-4V, Int. J. Impact Engineering 34 (2007) 771-783.

[51] T.W. Wright, The Physics and Mathematics of Adiabatic Shear Bands, Cambridge University Press, Cambridge (2002) 176-177.

[52] M.A. Meyers, A. Mishra, D.J. Benson, Mechanical properties of nanocrystalline materials. Prog. Mater. Sci. 51 (2006) 427-556.

[53] O. Bouaziz, Strain-Hardening of twinning-induced plasticity steels, Scripta Mater. 66 (2012) 982-985.

[54] N.R. Tao, K. Lu, Nanoscale structural refinement via deformation twinning in face-centered cubic metals, Scr. Mater. 60 (2009) 1039–1043.

[55] L. Lu, Z.S. You, K. Lu, Work hardening of polycrystalline Cu with nanoscale twins, Scr. Mater. 66 (2012) 837–842.

[56] C. Zener, J.H. Hollomon, Effect of strain rate upon plastic flow of steel, J. Appl. Phys. 15 (1944) 22–32.

[57] L.L. Zhu, S.X. Qu, X. Guo, J. Lu, Analysis of the twin spacing and grain size effects on mechanical properties in hierarchically nanotwinned face-centered cubic metals based on a mechanismbased plasticity model, J. Mech. Phys. Solids. 76 (2015) 162–179.

[58] L.L. Zhu, H.N. Kou, J. Lu, On the role of hierarchical twins for achieving maximum yield strength in nanotwinned metals, Appl. Phys. Lett. 101 (2012) 081906.

[59] X.L. Wu, Y.T. Zhu, Y.G. Wei, Q. Wei, Strong strain hardening in nanocrystalline nickel, Phys. Review Letters 103 (2009) 205504.

[60] V. Yamakov, D. Wolf, S.R. Phillpot, A.K. Mukherjee, H. Gleiter, Dislocation processes in the deformation of nanocrystalline aluminium by molecular-dynamics simulation, Nat. Mater. 1 (2002) 45–48.

[61] L. Dupuy, M.C. Fivel, A study of dislocation junctions in FCC metals by an orientation dependent line tension model, Acta Mater. 50 (2002) 4873-4885.

[62] W.W. Jin, G.M. Cheng, W.Z. Xu, H. Yuan, M.H. Tsai, Q.D. Wang, C.C. Koch, Y.T. Zhu, S.N. Mathaudhu, Ultrastrong Mg alloy via nano-spaced stacking faults. Mater. Res. Lett. **1** (2013) 61-66.

[63] J. Mao, C.E. Slone, T.M. Smith, C. Niu, H. Bei, M. Ghazisaeidi, G.M. Pharr, M.J. Mills, The evolution of the deformation substructure in a Ni-Co-Cr equiatomic solid solution alloy, Acta Mater. 132 (2017) 35-48.

[64] A. Mani, Salinas-Rodriguez, H.F. Lope, Deformation induced FCC to HCP transformation in a Co-27Cr-5Mo-0.05C alloy, Mater. Sci. Eng. A 528 (2011) 3037-3043.

[65] O. Grassel, L. Kruger, G. Frommeyer, High strength Fe-Mn-(Al, Si) TRIP/TWIP steels development - properties - application, Int. J. Plast. **16** (2000) 1391-1409.

[66] X.L. Wu, Y.T. Zhu, Heterogeneous materials: a new class of materials with unprecedented

mechanical properties, Mater. Res. Lett. **5** (2017) 527-532.

[67] E. Ma, T. Zhu, Towards strength-ductility synergy through the design of heterogeneous nanostructures in metals, Mater. Today **20** (2017) 323-331.

[68] R.D. Pehlke, A. Jeyarajan, H. Wada, Summary of thermal properties for casting alloys and mold materials, University of Michigan (1982).

[69] Y.L. Bai, B. Dodd, Adiabatic Shear Localization, Pergamon Press, New York (1992).

[70] T.W. Wright, The Physics and Mathematics of Adiabatic Shear Bands, Cambridge University Press, Cambridge (2002) 176–177.

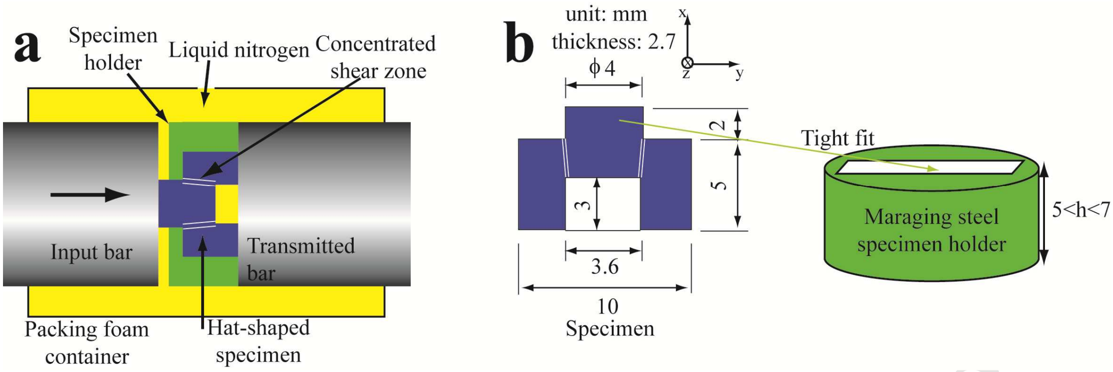
a
Specimen holder
Liquid nitrogen
Concentrated shear zone
Input bar
Transmitted bar
Packing foam container
Hat-shaped specimen
b
unit: mm
thickness: 2.7
x
z
y
ϕ 4
2
5
3
3.6
10
Specimen
Tight fit
Maraging steel specimen holder
5<h<7

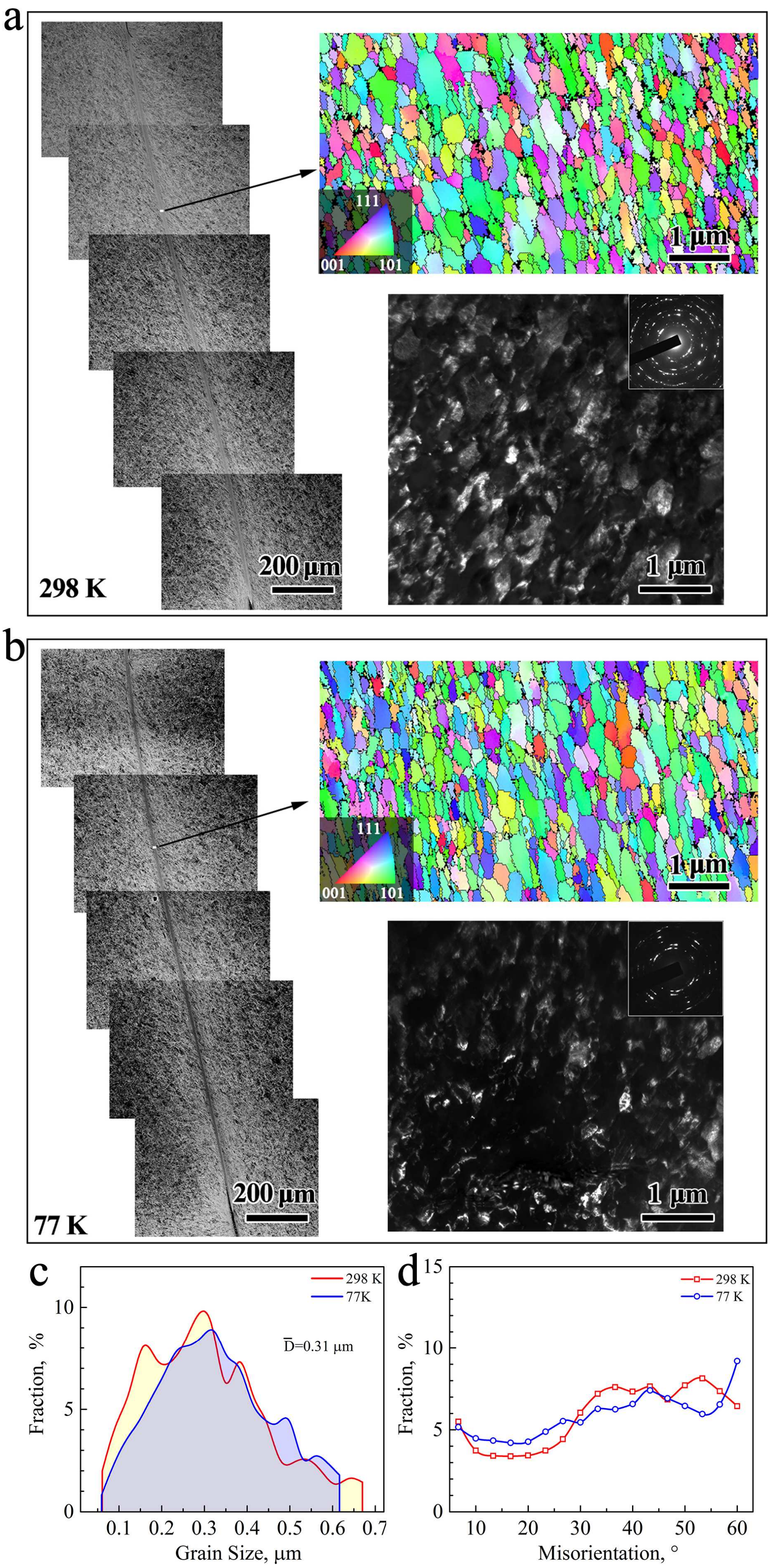
a
111
001
101
1 μm
200 μm
1 μm
298 K
b
111
001
101
1 μm
200 μm
1 μm
77 K
c
Fraction, %
Grain Size, μm
298 K
77K
D̄=0.31 μm
0
5
10
0.1
0.2
0.3
0.4
0.5
0.6
0.7
d
Fraction, %
Misorientation, °
298 K
77 K
0
5
10
15
10
20
30
40
50
60

RIPT

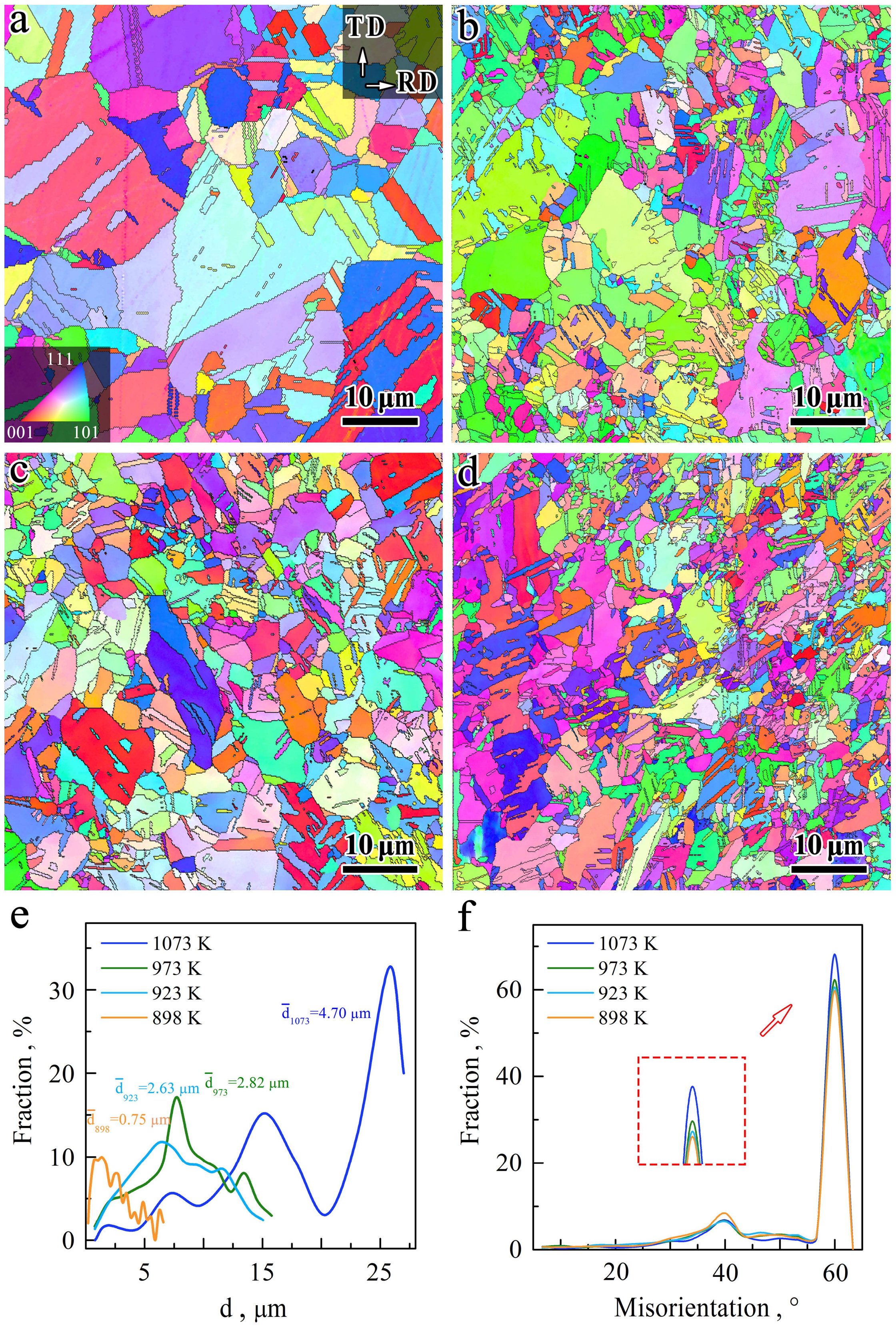
a
TD
RD
111
001
101
10 µm
b
10 µm
c
10 µm
d
10 µm
e
1073 K
973 K
923 K
898 K
d̄1073=4.70 µm
d̄923=2.63 µm
d̄973=2.82 µm
d̄898=0.75 µm
Fraction , %
0
10
20
30
5
15
25
d , µm
f
1073 K
973 K
923 K
898 K
Fraction , %
0
20
40
60
20
40
60
Misorientation , °

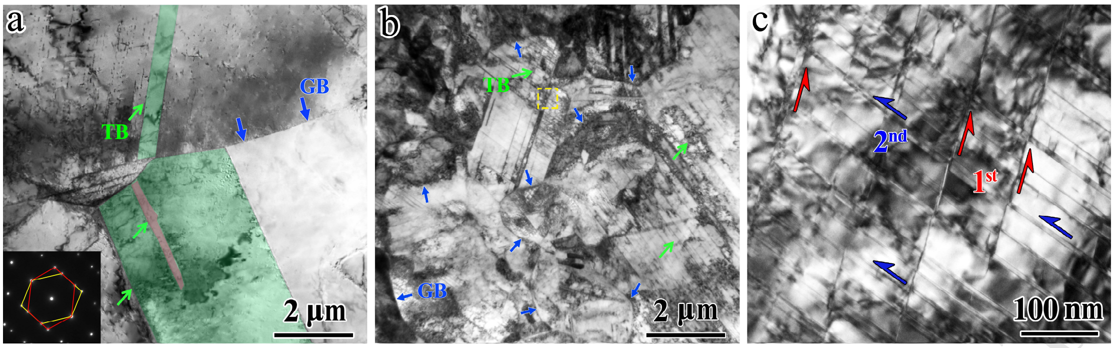
a
TB
GB
2 µm
b
TB
GB
2 µm
c
2nd
1st
100 nm

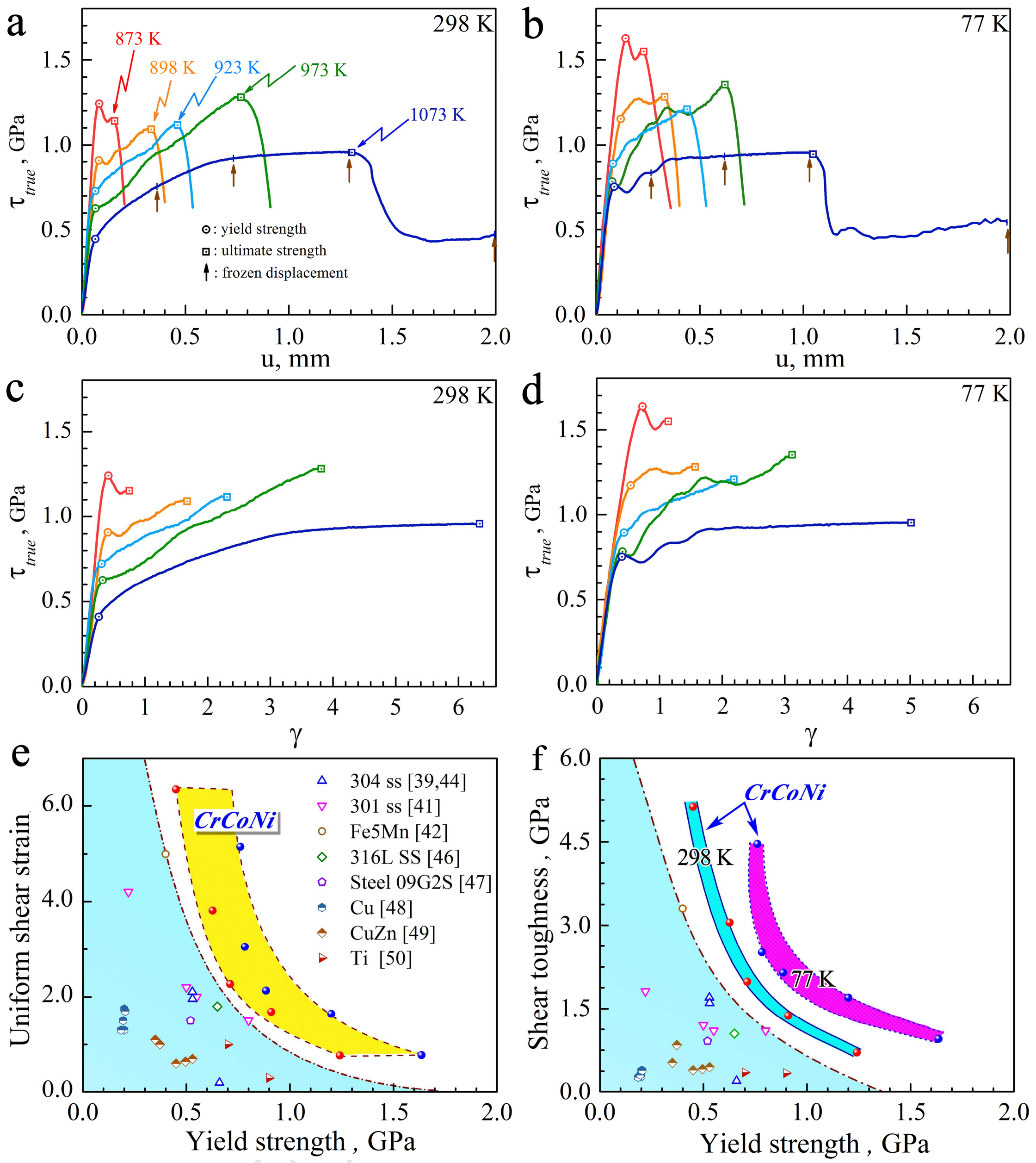
a
298 K
873 K
898 K
923 K
973 K
1073 K
⊙ : yield strength
⊡ : ultimate strength
↑ : frozen displacement
τtrue , GPa
u, mm
0.0
0.5
1.0
1.5
2.0
b
77 K
c
298 K
γ
0
1
2
3
4
5
6
d
77 K
e
CrCoNi
304 ss [39,44]
301 ss [41]
Fe5Mn [42]
316L SS [46]
Steel 09G2S [47]
Cu [48]
CuZn [49]
Ti [50]
Uniform shear strain
Yield strength , GPa
f
CrCoNi
298 K
77 K
Shear toughness , GPa
Yield strength , GPa
0.0
1.5
3.0
4.5
6.0

ACCE

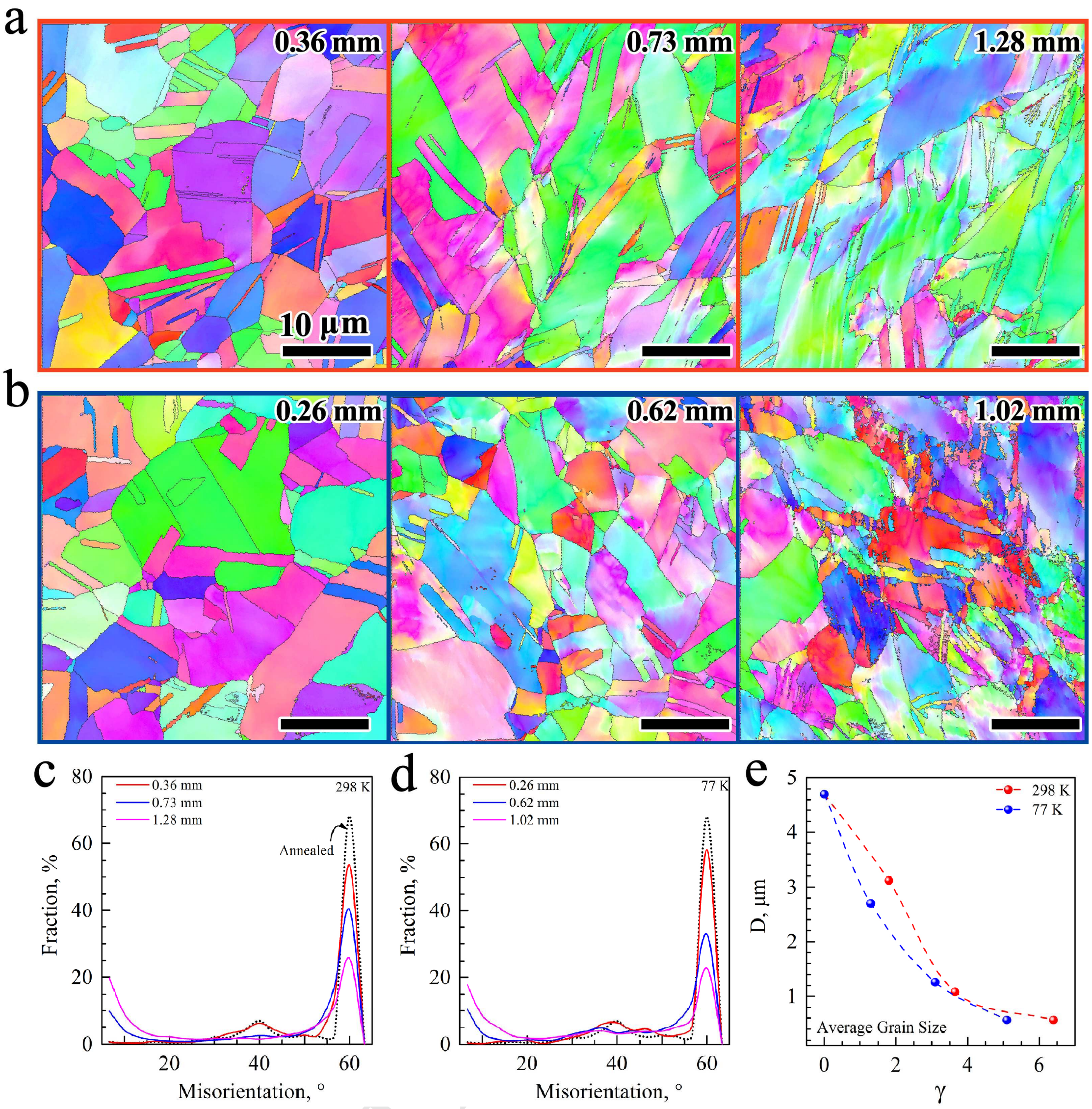
a
0.36 mm
0.73 mm
1.28 mm
10 µm
b
0.26 mm
0.62 mm
1.02 mm
c
0.36 mm
0.73 mm
1.28 mm
298 K
Annealed
Fraction, %
Misorientation, °
0
20
40
60
80
d
0.26 mm
0.62 mm
1.02 mm
77 K
Fraction, %
Misorientation, °
e
298 K
77 K
D, µm
Average Grain Size
γ
0
2
4
6
1
3
5

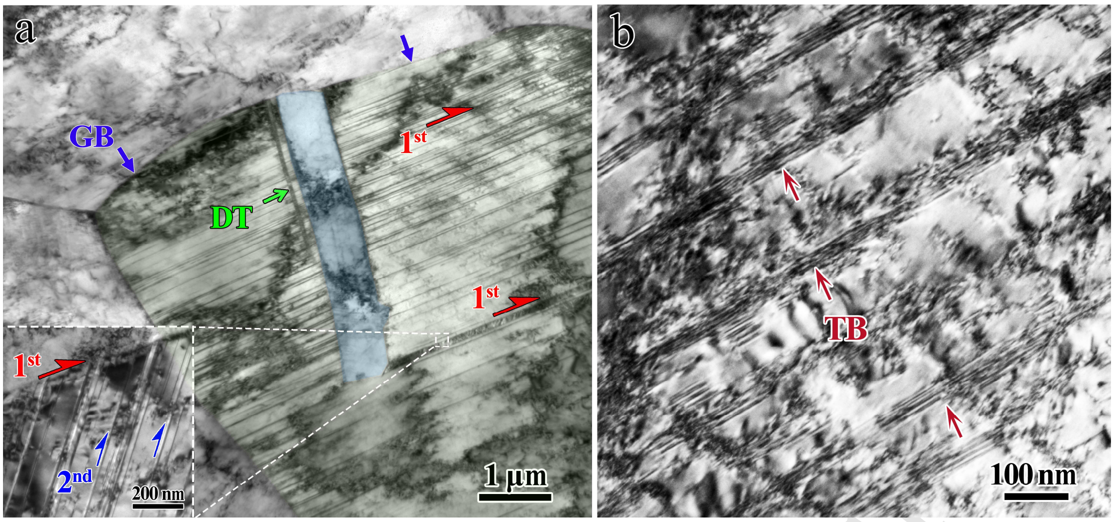
a
GB
DT
1st
1st
1st
2nd
200 nm
1 μm
b
TB
100 nm

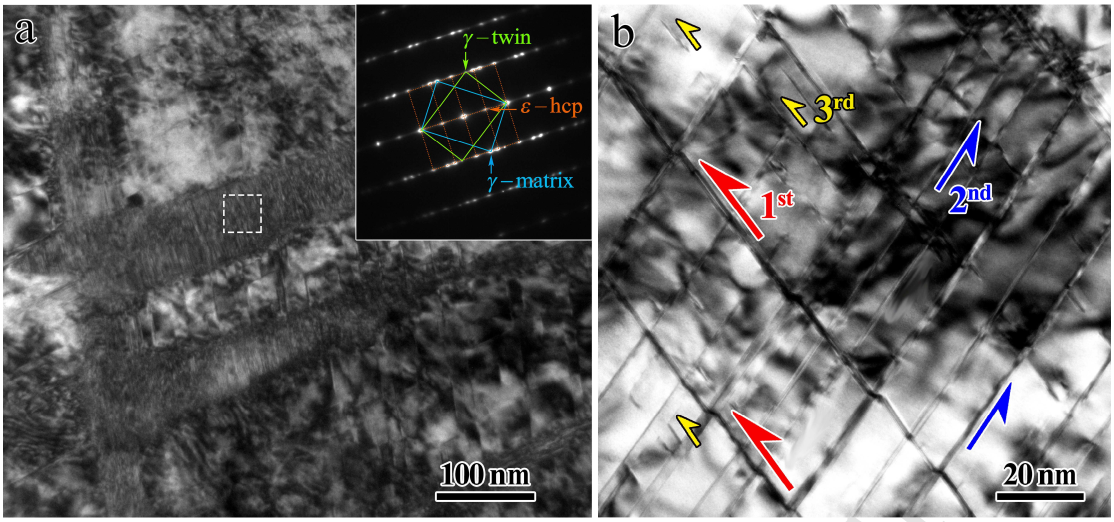
a
γ – twin
ε – hcp
γ – matrix
100 nm
b
3rd
1st
2nd
20 nm

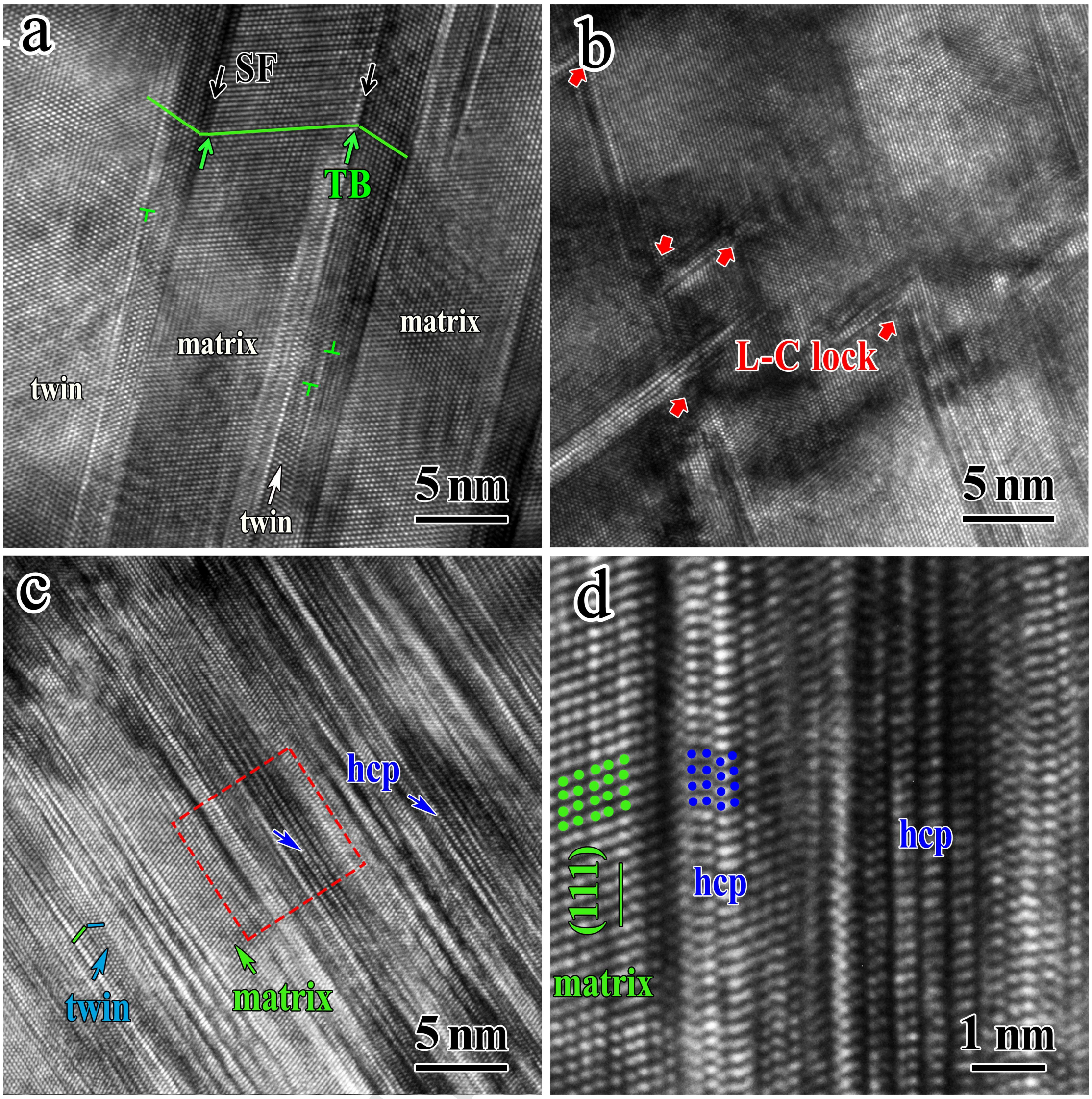
a
SF
TB
matrix
matrix
twin
twin
5 nm
b
L-C lock
5 nm
c
hcp
twin
matrix
5 nm
d
hcp
hcp
(111)
matrix
1 nm

ACCEPTED

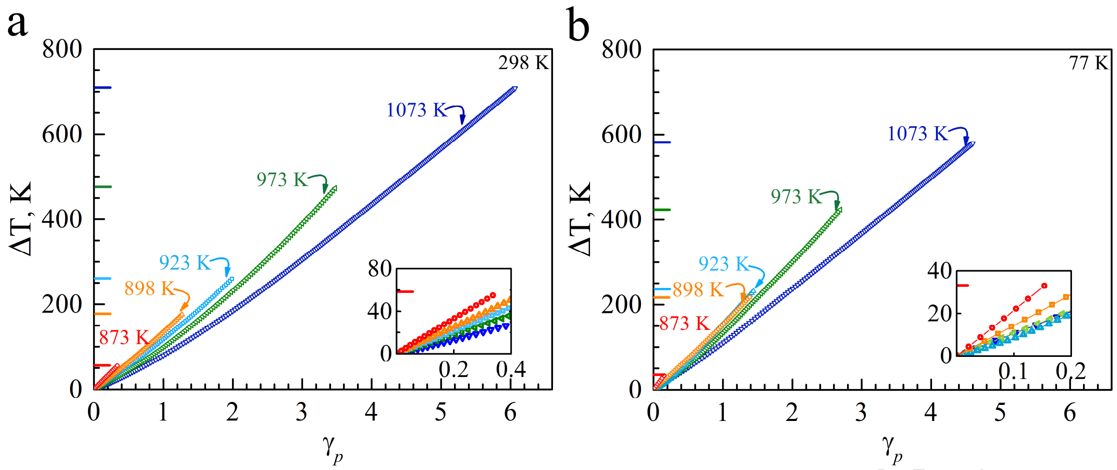
a
800
600
400
200
0
ΔT, K
298 K
1073 K
973 K
923 K
898 K
873 K
0
1
2
3
4
5
6
γ_p
80
40
0
0.2
0.4
b
800
600
400
200
0
ΔT, K
77 K
1073 K
973 K
923 K
898 K
873 K
0
1
2
3
4
5
6
γ_p
40
20
0
0.1
0.2

Figures and captions

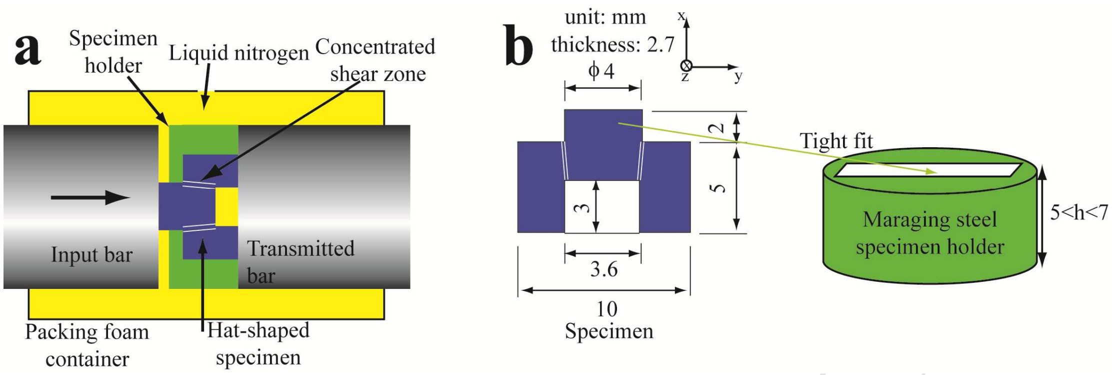
a
Specimen holder
Liquid nitrogen
Concentrated shear zone
Input bar
Transmitted bar
Packing foam container
Hat-shaped specimen
b
unit: mm
thickness: 2.7
ϕ 4
x
y
z
2
5
3
3.6
10
Specimen
Tight fit
Maraging steel specimen holder
5<h<7

Fig. 1 (a) Hat-shaped specimen set-up in Hopkinson bar experiment; (b) Illustrations and dimensions of the hat-shaped specimen and the specimen holder.

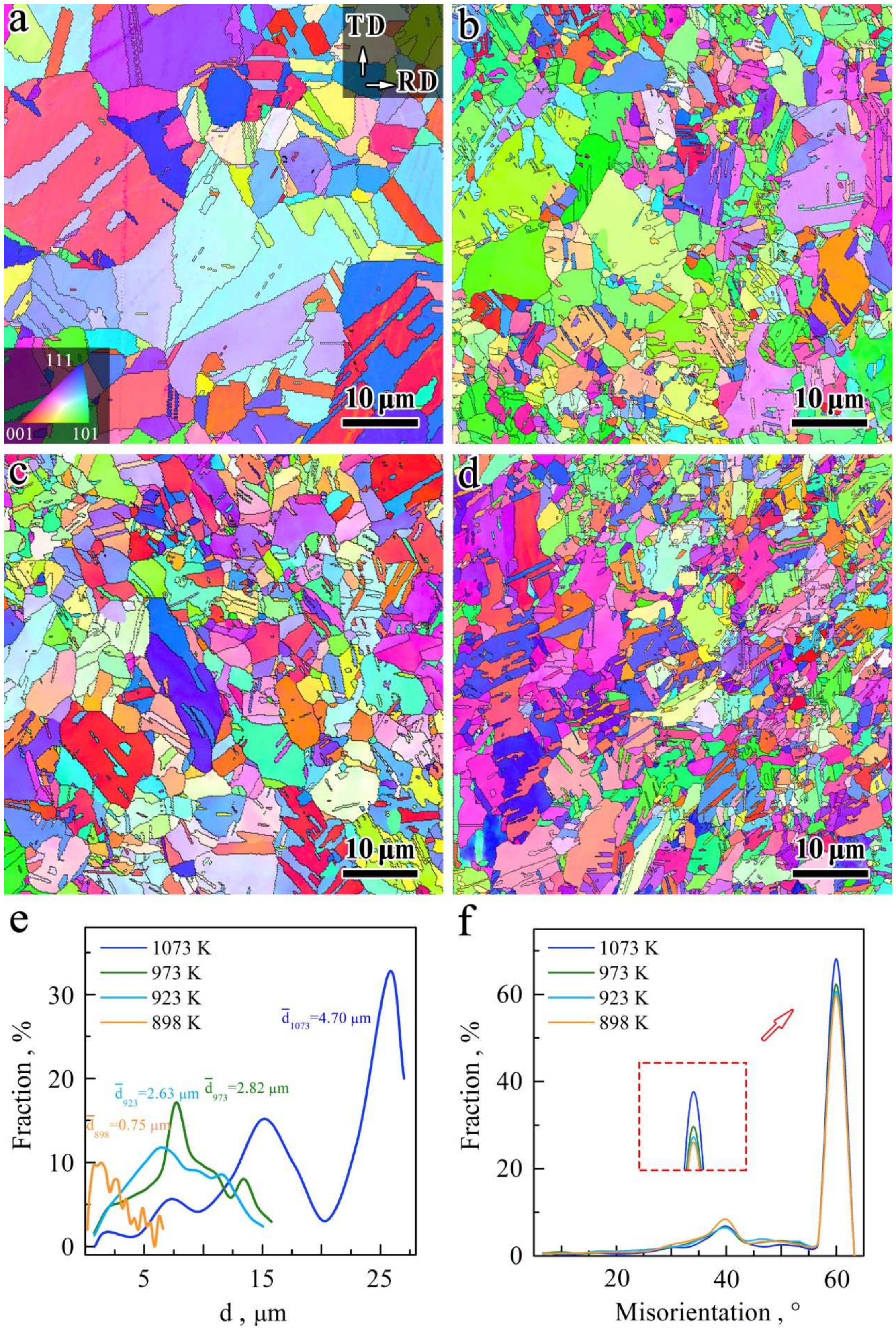

Fig. 2 (a) IPF map for the microstructure annealed at 1073 K; (b) IPF map for the microstructure annealed at 973 K; (c) IPF map for the microstructure annealed at 923 K; (d) IPF map for the microstructure annealed at 898 K; (e) The corresponding grain size distributions for various microstructures, plotted in terms of the area fraction; (f) The corresponding misorientation angle distributions for various microstructures.

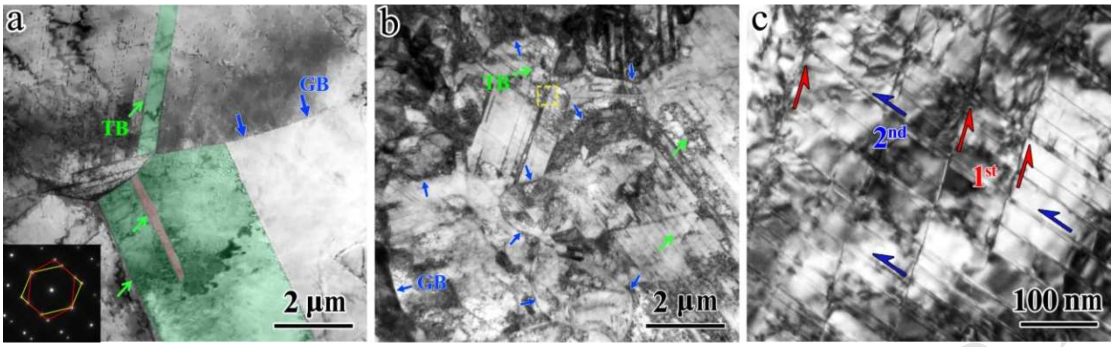
a
TB
GB
2 μm
b
TB
GB
2 μm
c
2nd
1st
100 nm

Fig. 3 (a) TEM bright-field image for the microstructure annealed at 1073 K; (b) TEM bright-field image for the microstructure annealed at 898 K; (c) The corresponding close-up view for the rectangular area in (b).

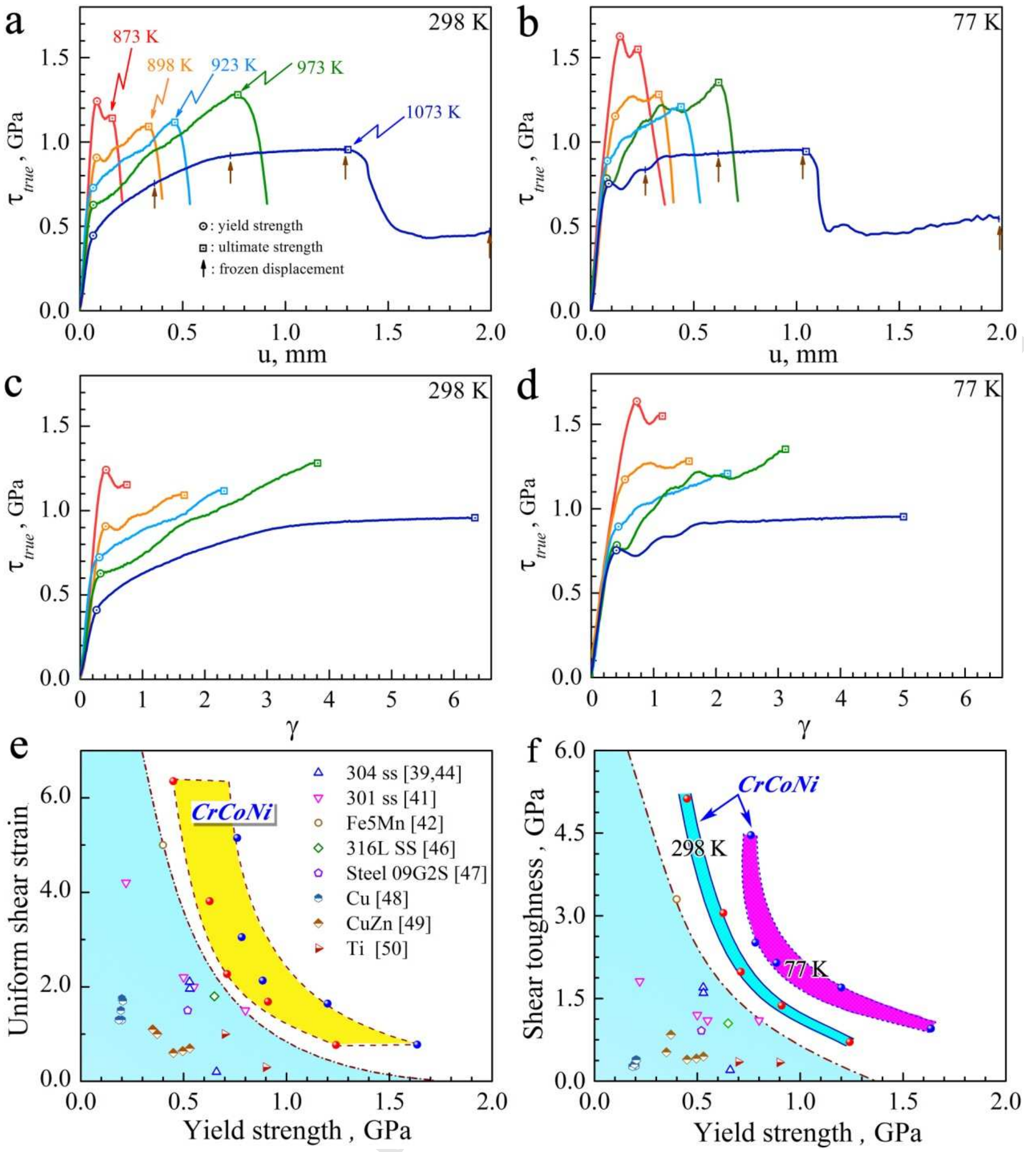

Fig. 4 Shear stress-shear displacement curves of various microstructures for the experiments conducted: (a) at room temperature; (b) at cryogenic temperature. Shear stress-nominal shear strain curves of various microstructures for the experiments conducted: (c) at room temperature; (d) at cryogenic temperature. (e) Uniform dynamic shear strain vs. dynamic shear yield strength for the present MEA, along with the data for other metals and alloys. (f) Impact shear toughness vs. dynamic shear yield strength for the present MEA, along with the data for other metals and alloys.

ACCEPTED

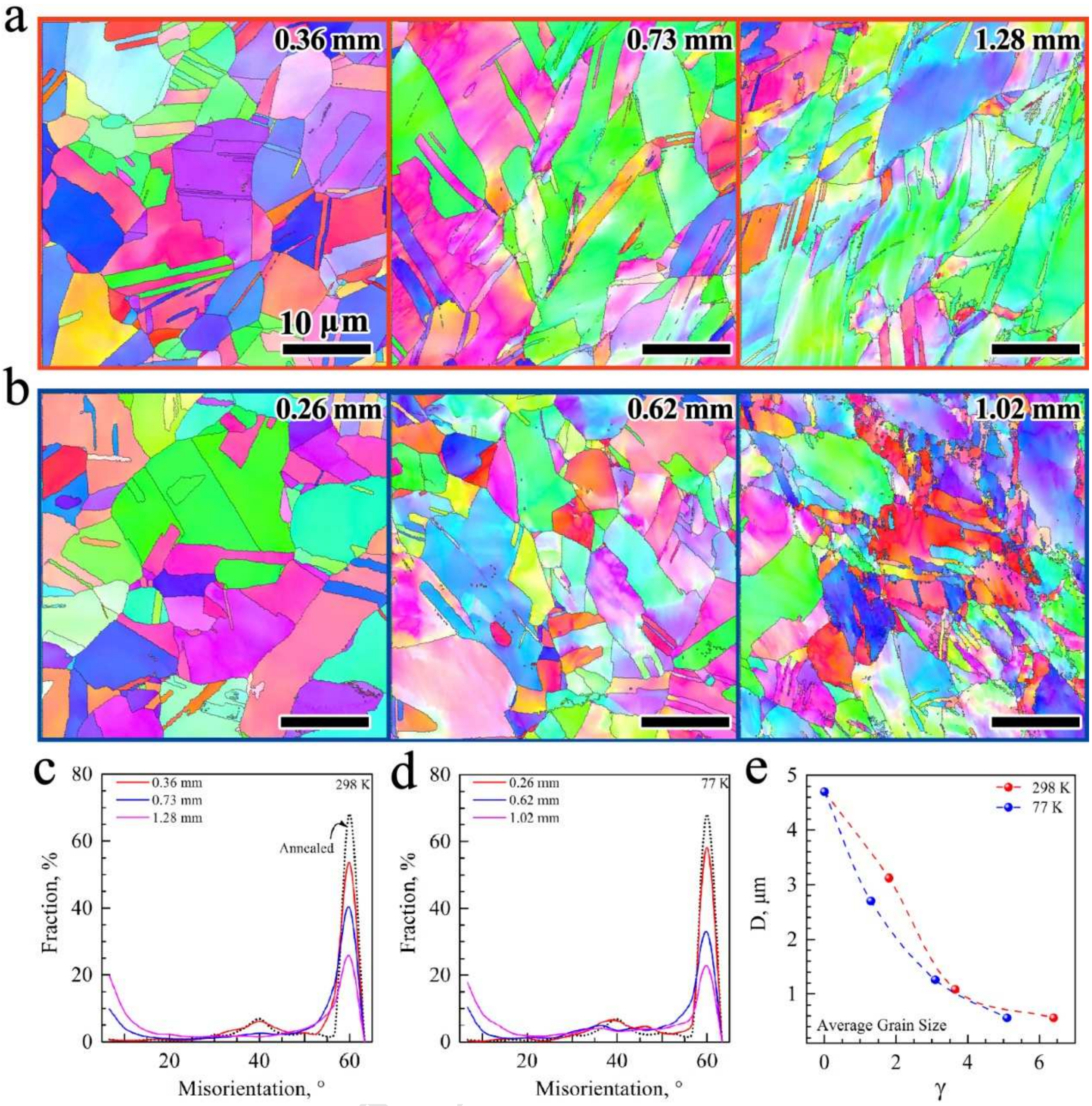

Fig. 5 The IPF images of the sample annealed at 1073 K at various shear displacements for the experiments conducted: (a) at room temperature; (b) at cryogenic temperature. The corresponding misorientation angle distributions at various shear displacements for the experiments conducted: (c) at room temperature; (d) at cryogenic temperature. (e) The grain size as a function of the homogeneous shear strain for the experiments conducted at both room temperature and cryogenic temperature.

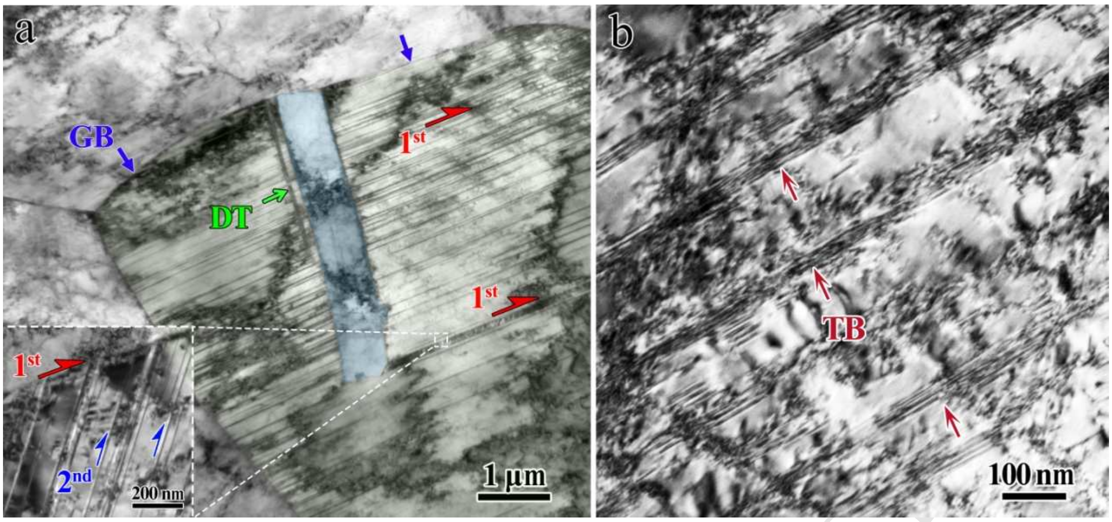
a
GB
DT
1st
1st
1st
2nd
200 nm
1 μm
b
TB
100 nm

Fig. 6 TEM bright-field images of the homogeneous shear deformation zone for the experiments conducted at room temperature: (a) showing DTs; (b) showing accumulation of high density of dislocation at TBs.

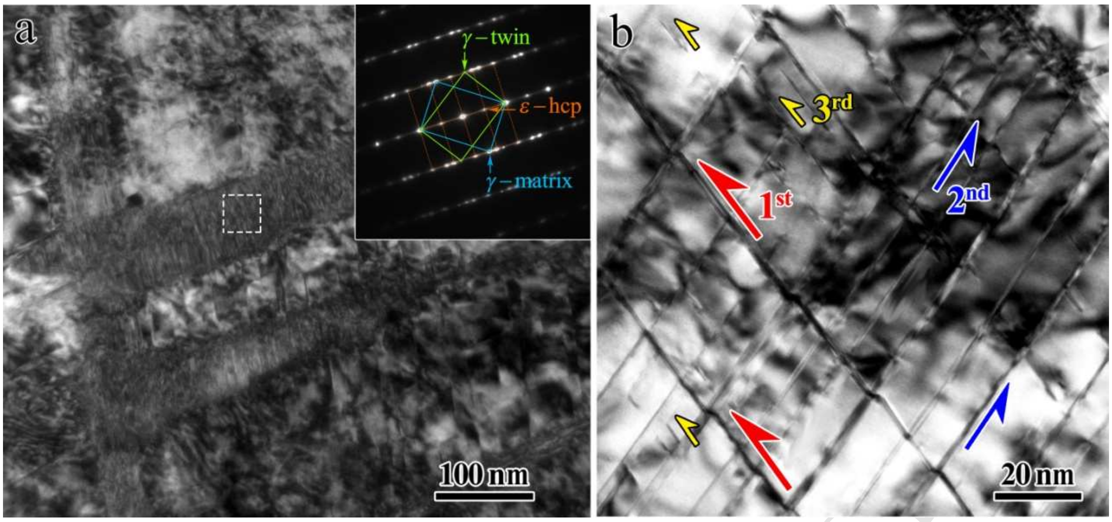
a
γ−twin
ε−hcp
γ−matrix
100 nm
b
3rd
1st
2nd
20 nm

Fig. 7 TEM bright-field images of the homogeneous shear deformation zone for the experiments conducted at cryogenic temperature: (a) showing high density of SFs and phase transformation; (b) showing multiple DTs.

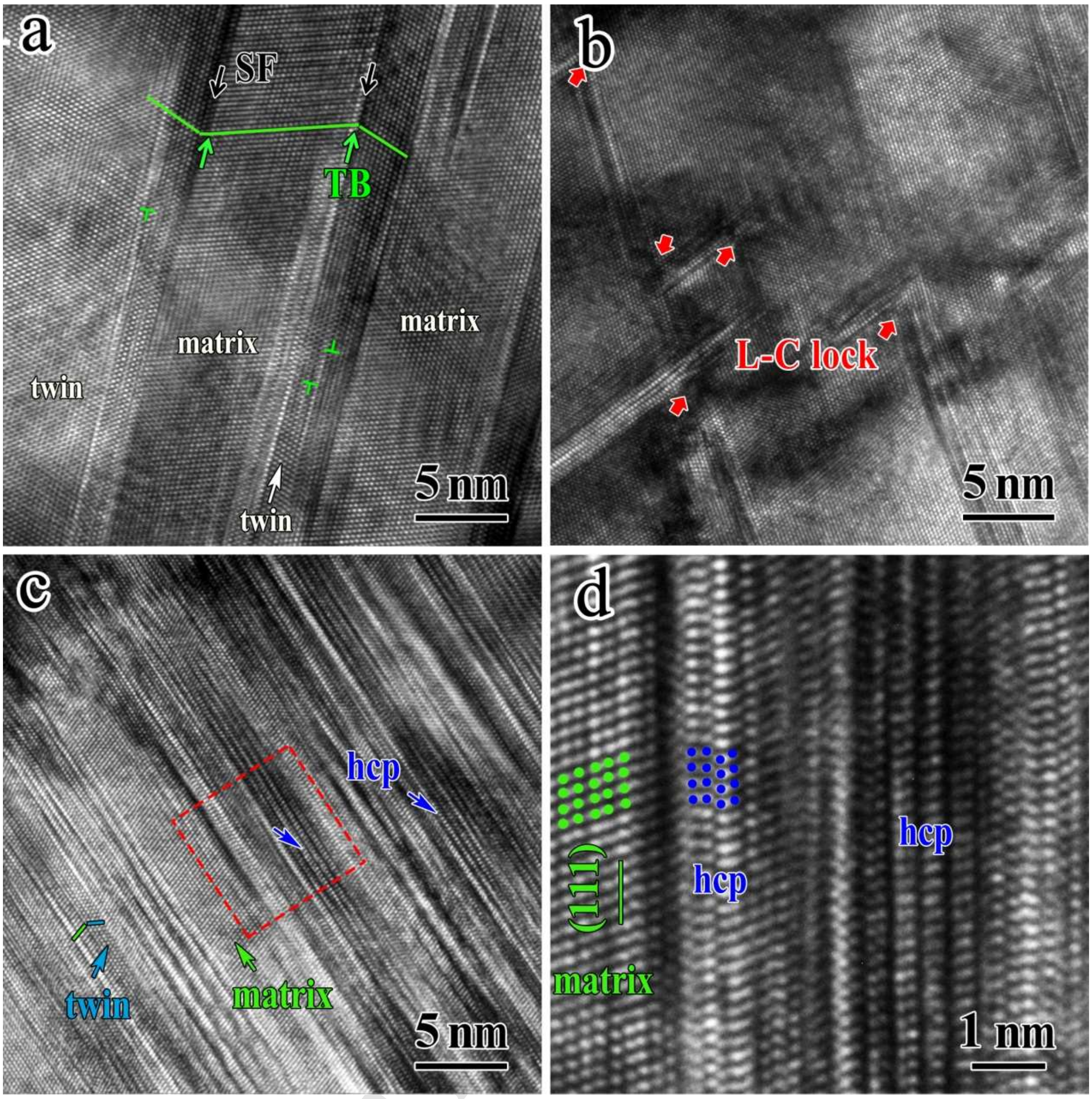
a
SF
TB
matrix
matrix
twin
twin
5 nm
b
L-C lock
5 nm
c
hcp
twin
matrix
5 nm
d
hcp
hcp
(111)
matrix
1 nm

Fig. 8 HREM images of the homogeneous shear deformation zone for the experiments conducted at cryogenic temperature: (a) showing TBs, SFs and dislocations at TBs ; (b) showing L-C locks; (c) showing high density of SFs and phase transformation; (d) the close-up view of the rectangle area in (c) for the details of hcp phase.

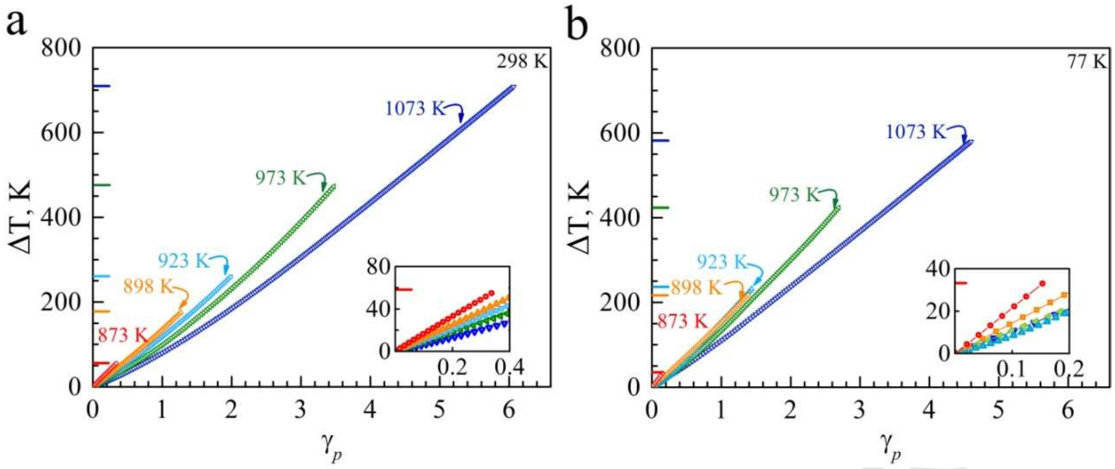

Fig. 9 The temperature rise vs. the homogeneous shear strain curves for the experiments conducted: (a) at room temperature; (b) at cryogenic temperature.

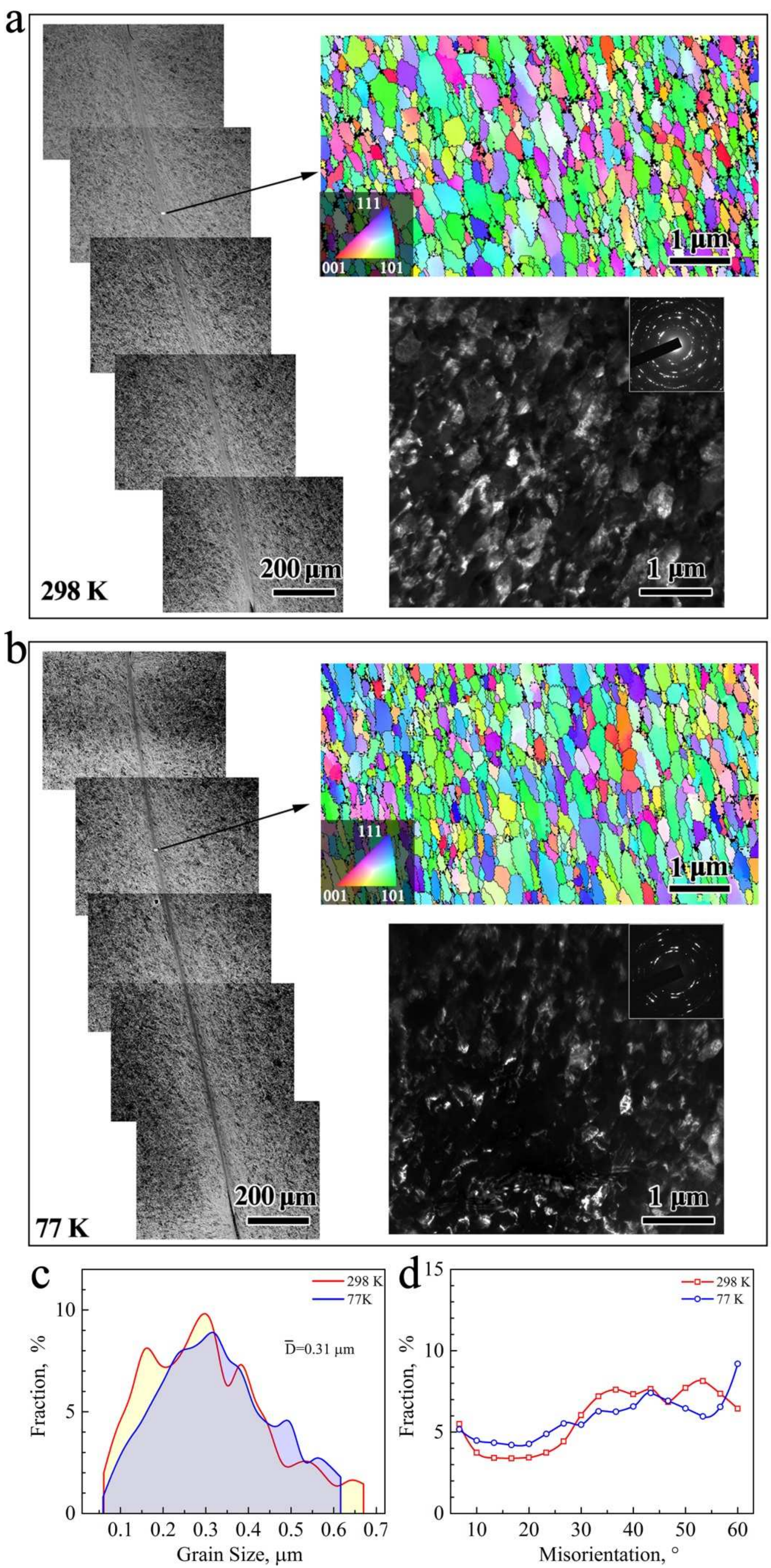
a
111
001
101
1 µm
1 µm
200 µm
298 K
b
111
001
101
1 µm
1 µm
200 µm
77 K
c
298 K
77K
D̄=0.31 µm
Fraction, %
Grain Size, µm
0
5
10
0.1
0.2
0.3
0.4
0.5
0.6
0.7
d
298 K
77 K
Fraction, %
Misorientation, °
0
5
10
15
10
20
30
40
50
60

Fig. 10 The characteristics of the ASB (SEM, EBSD and TEM images) at the shear displacement of 2.0 mm for the sample annealed at 1073 K and for the experiment: (a) conducted at room temperature; (b) conducted at cryogenic temperature. (c) The grain size distributions within ASB for the experiments conducted both at room temperature and cryogenic temperature. (d) The corresponding misorientation angle distributions of ASB zone for the experiments conducted both at room temperature and cryogenic temperature.